Stiffness Reduction of Flexure Pivots using Fixed-Lever Buckled Beams

Loïc Tissot-Daguette, Guillaume Lods, Simon Henein

Micromechanical and Horological Design Laboratory (Instant-Lab)
École Polytechnique Fédérale de Lausanne (EPFL), Rue de la Maladière 71, Neuchâtel, 2000, NE, Switzerland

E-mail address: loic.tissot-daguette@epfl.ch

Keywords: Compliant Mechanisms, Flexure Pivots, Stiffness Tuning, Zero Stiffness, Static Balancing, Beam Buckling, Multistability, Residual Stress

Abstract

Stiffness reduction of compliant mechanisms has become an important research topic. Although numerous strategies have been proposed for flexure-based linear stages, design methods exploiting beam buckling to reduce the angular stiffness of flexure pivots remain scarce. This paper introduces a buckling-based mechanism consisting of two beams clamped at one end and attached to a rotating lever at the other. We refer to this support condition as fixed-lever, distinguishing it from the conventional fixed-pinned configuration. Analytical and numerical investigations show that a single fixed-lever buckled beam exhibits highly nonlinear and hysteretic behavior under rotational actuation. However, pairing two such beams and enforcing symmetric buckling yields a nearly constant negative angular stiffness near the neutral position. This negative-stiffness structure can be monolithically integrated into generic flexure pivots to reduce their angular stiffness. Closed-form analytical formulas are derived to guide the design of targeted stiffness-reduction profiles. The concept and analytical model are validated through finite element simulations and experiments on metal and additively manufactured polymer prototypes. Finally, microscale silicon pivots preloaded through thermal oxidation achieve a measured stiffness reduction of 96% over an operating range of ± 4.5 deg.

1 Introduction

Compliant and flexure-based mechanisms have gained significant attention across precision engineering disciplines due to their inherent advantages over traditional rigid-body mechanisms (Henein, 2000; Howell, 2001; Smith, 2000). By relying on elastic deformation rather than discrete joints, flexure mechanisms enable motion without friction, backlash, or wear, and offer high precision, compactness, and the possibility

for monolithic designs. In recent years, these mechanisms have also been studied for their ability to modify stiffness profiles (Arredondo-Soto et al., 2021; Pan et al., 2025; Wen and Wu, 2025). More specifically, the stiffness of flexure mechanisms can be tuned or adjusted by prestressing some of their flexures (Mauser and Hasse, 2020; Mauser et al., 2022; de Laat et al., 2016; Amoozandeh Nobaveh et al., 2024; Parkinson et al., 2025; Blad et al., 2021).

Research on stiffness-engineered compliant mechanisms has expanded rapidly, with applications ranging from micro-electromechanical systems (MEMS) (Halg, 1990; Hussein et al., 2024, 2020; Qiu et al., 2004; Saif, 2000; Yang et al., 2007), shock and vibration isolation systems (Ma et al., 2022; Yu et al., 2025), minimally invasive medical tools (Niazi et al., 2026; Zanaty et al., 2019), aerospace systems (Barri et al., 2025; Zirbel et al., 2016), to bio-inspired soft robots (Chao et al., 2024; Chen et al., 2018; Chi et al., 2022; Tang et al., 2020). Within these domains, mechanisms that exhibit static balancing, near-zero stiffness behavior, or bistability offer compelling benefits, including reduced actuation effort, improved energy efficiency, enhanced sensitivity, and the ability to passively maintain multiple stable configurations. To achieve such behaviors, various preload strategies have been proposed in the literature, where gravity (Barents et al., 2011), preloaded springs (Liu et al., 2020; Morsch and Herder, 2011; Smreczak et al., 2022; Wu and Lan, 2014; Yang et al., 2020; Zanaty et al., 2018; Zhao et al., 2019, 2017), and post-buckled beams (Kuppens et al., 2021a, 2021b, 2019; Numić et al., 2021; Tissot-Daguette et al., 2025, 2024b) are used to modify the natural stiffness of compliant mechanisms.

Most state-of-the-art gravity-orientation independent solutions based on preloaded springs for stiffness reduction require complex assemblies rather than monolithic designs, reducing practicality for microscale applications. Buckled beams, on the other hand, can easily be incorporated into flexure mechanisms as they only require a small number of elements and allow for monolithic design using in-situ stress in microscale systems (Kuppens et al., 2019; Tissot-Daguette et al., 2025; Vangbo and Bäcklund, 1998). However, they are quite complex to model and design due to stiffness nonlinearities, which drastically vary depending on their boundary conditions and potential initial curvature (Liu and Hao, 2025; Pan et al., 2022; Parkinson et al., 2025; Yang et al., 2007).

Even though numerous solutions based on beam post-buckling have been proposed in the literature for stiffness reduction of flexure linear stages, e.g., by incorporating fixed-guided buckled beams (Dijksman, 1979; Kuppens et al., 2021a, 2021b, 2019; Liang et al., 2022; Numić et al., 2021; Tissot-Daguette et al., 2025, 2022a), relatively few structures exist that effectively reduce the angular stiffness of flexure pivots. Bilancia et al. (2020) propose to incorporate centered pinned-pinned buckled beams in an Archimedean spiral compliant pivot for angular stiffness reduction. Kuppens et al. propose to reduce the stiffness of flexure pivots using either two off-centered V-shaped

buckled beams (Kuppens et al., 2021a) or two constant-torque mechanisms based on pre-curved buckled beams (Kuppens et al., 2021b).

The response of post-buckled-beam pivot architectures depends not only on boundary conditions and potential initial curvature, but also on the relative positioning of the buckled beams' extremities with respect to the pivot axis, which introduces lever-arm effects. In particular, when post-buckled beams do not intersect at the pivot point, secondary lever-arm effects arise that can substantially alter the resulting angular stiffness. These effects remain poorly quantified in the literature and complicate the predictive synthesis of stiffness-reduced pivots.

In this paper, we introduce a new angular-stiffness-reduction architecture based on two centered, initially straight post-buckled beams rigidly connected in parallel between a fixed frame and a rotating stage. A lever-arm distance is intentionally introduced between the rotating beam extremities and the pivot axis. When the buckling beams buckle in opposite directions and with equal preloading displacement, the proposed architecture generates a negative stiffness that can advantageously reduce the angular stiffness of generic flexure pivots.

The main contributions of this work are threefold. First, we derive a simplified closed-form analytical model describing the moment-angle behavior of single and paired post-buckled beams, enabling the desired stiffness compensation to be designed predictably in a single step rather than through iterative tuning. Second, by identifying and quantifying the role of lever-arm distance, we show that this geometric parameter strongly influences the achievable stiffness reduction and angular stroke. Third, we model the case in which the axes of two buckled beams are offset relative to the pivot center, thereby clarifying a secondary lever-arm effect that substantially modifies the resulting angular stiffness. Together, these contributions establish analytical design rules for stiffness-reduced flexure pivots and provide a predictive framework for their synthesis.

These conceptual contributions are illustrated through two representative state-of-the-art flexure pivots—cross-spring pivots and remote-center-of-compliance (RCC) pivots—and demonstrated for the realization of common stiffness behaviors, namely monostable (positive stiffness), statically balanced (near-zero stiffness), and bistable (negative stiffness) responses. Under certain configurations, tristable behavior is also demonstrated.

The remainder of this paper is organized as follows. Section 2 presents the conceptual structure of the mechanism and its working principle. To enable systematic design, we derive an analytical model for the moment-angle characteristics of a single buckled beam and the assembly of two buckled beams, in Secs. 3.1 and 3.2, respectively. Then, metal and plastic mockups, as well as micro-scale silicon prototypes are designed in Sec. 4. Section 5 presents finite element model (FEM) simulations and experiments

used to validate the analytical model and the design of the mechanisms. The results presented in Sec. 6 support the conclusion in Sec. 7 that the preloading strategy successfully reduces flexure pivot stiffness across different materials and scales.

2 Conceptual description

The new negative-stiffness pivot proposed in this paper is shown in Figs. 1a to 1c. It consists of a rotating stage mounted on an input pivot and connected to two buckling beams of length L, each preloaded by a linear-motion preloading stage. In the neutral position (Fig. 1a), the longitudinal axes of the buckling beams intersect at the center of rotation of the rotating stage. Although the two beams are shown perpendicular to each other in Fig. 1a, this specific orientation is not required; any angle between the beams is admissible. The lever length p is defined as the distance between the pivot's center of rotation and the connected extremity of the beam. The preloading stages apply an equal longitudinal displacement Δx to both beams to induce buckling (Fig. 1b). When the pivot is rotated by an angle θ_{in} (Fig. 1c), the two buckling beams jointly generate a reaction moment $M_{\text{in,2beams}}$ acting on the rotating stage.

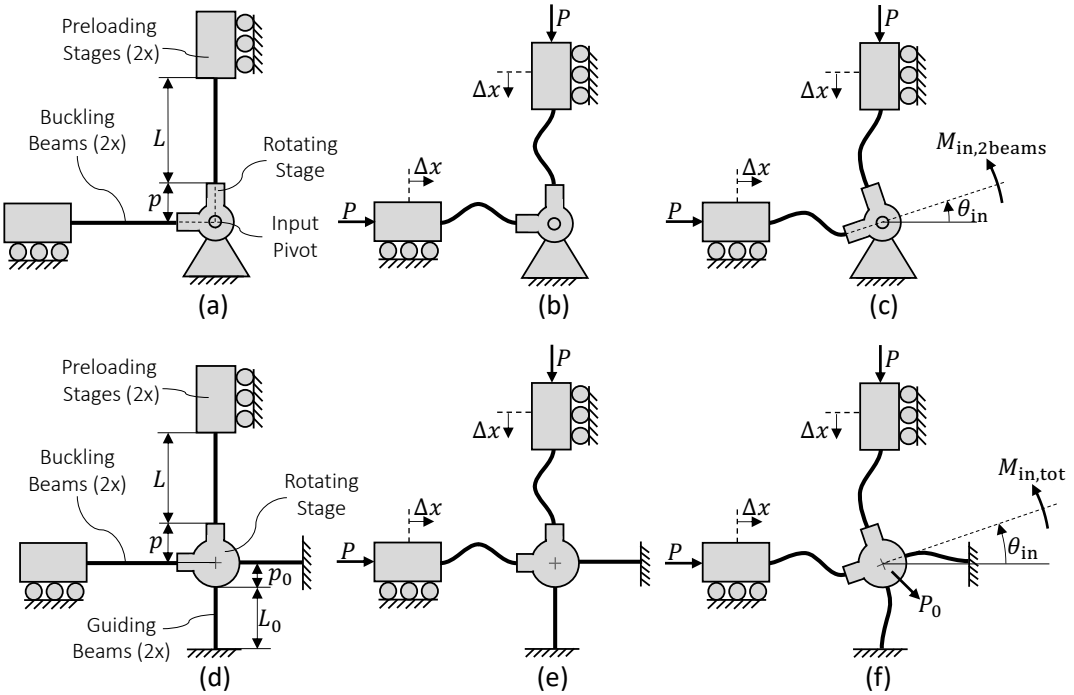

Figure 1. Pivot preloaded by two fixed-lever buckled beams (a) as-fabricated, (b) in neutral position, (c) rotated, and (d-e) mechanism in (a-c) where the pivot is embodied using flexures.

The load case of each buckling beam differs from the conventional *fixed-pinned* boundary condition, in which the center of rotation of the rotating end coincides exactly with the beam extremity. To avoid confusion, we refer to the present support configuration as *fixed-lever*, since a distance p separates the beam extremity from the

center of rotation (see Fig. 1a). The modeling in Sec. 3 shows that combining two fixed-pinned buckled beams with opposite buckling directions would yield a positive stiffness, rather than the desired negative stiffness. Indeed, only specific lever length ratios $\bar{p} = p/L$ can reduce the angular stiffness. In Sec. 3.2.4, we will see that the angular stroke where the negative stiffness remains approximately constant also depends on the ratio $\bar{p}$.

In contrast to fixed-guided buckled beams, where a single beam is sufficient to generate negative stiffness for a linear stage, a single fixed-lever buckled beam cannot produce negative stiffness. This is because fixed-pinned buckled beams introduce a moment offset in the neutral position (Tissot-Daguette et al., 2022b). To compensate for this offset, the proposed solution employs two buckling beams that deform in opposite directions and are preloaded by an equal displacement Δx. Under this condition, the resulting moment-angle characteristic exhibits negative stiffness, governed by the chosen values of p and L.

The input pivot can be realized using a flexure pivot, such as an RCC pivot based on two guiding beams, as illustrated in Figs. 1d to 1f. Depending on the dimensions of the guiding and buckling beams, the resulting total stiffness $M_{\text{in,tot}}/\theta_{\text{in}}$ can be tuned to positive values (stiffness tuning), near-zero values (static balancing), or negative values (bistability). The entire mechanism can be fabricated monolithically if the preloading stages are also implemented using flexures.

Note that the stiffness-reduction principle applies regardless of whether the flexure pivot exhibits a parasitic shift or a near-zero parasitic shift (Spanoudakis et al., 2019; Thalmann and Henein, 2022; Tissot-Daguette et al., 2024a). However, it is worth noting that the potential parasitic shift must be considered when evaluating the stiffness reduction (see Sec. 3.2.2). The parasitic shift may also affect the flexure pivot's operational stroke by altering the effective precompression displacement of the buckling beams.

3 Analytical modeling

We analytically model the actuation characteristics of a single fixed-lever buckled beam in Sec. 3.1. This model is then used to determine the total stiffness of a flexure pivot preloaded by two fixed-lever buckled beams in Sec. 3.2. Throughout the analysis, gravity and dynamic effects are assumed negligible, the beams are considered initially straight, and their deformations are treated as sufficiently small to justify the use of Euler-Bernoulli beam theory.

3.1 Single fixed-lever buckled beam

Figure 2 shows the load case of one of the buckling beams of the mechanism illustrated in Fig. 1. The beam of length L is clamped at one end and connected to the input pivot via a lever of length p at the other extremity (see Fig. 2a). The lever is hinged to a preloading stage allowing the beam to be maintained in a buckled state when a horizontal displacement Δx is applied. Note that any vertical displacement, for example, due to a potential parasitic shift of the flexure pivot, is neglected in this model. The two symmetric stable equilibria of the buckling beam are illustrated in Fig. 2b. In Fig. 2c, the buckled beam is actuated in rotation at the input pivot by a controlled moment $M_{\text{in,1beam}}$ or by a controlled angle θ_{in}.

3.1.1 Actuation characteristics

The input stiffness $K_{\text{in,1beam}} = M_{\text{in,1beam}}/\theta_{\text{in}}$ of a fixed-lever buckled beam is given by previous work (Tissot-Daguette et al., 2021) as:

$$K_{\text{in,1beam}} = \frac{EI}{L} kL \frac{kL\cos(kL) - \sin(kL)\,(1 + (kL)^2\bar{p} + (kL)^2\bar{p}^2)}{kL\sin(kL) + 2(\cos(kL) - 1)} \tag{1}$$

where $k = \sqrt{P/EI}$, $\bar{p} = p/L$, EI is the flexural rigidity and L is the beam length. The input angle θ_{in} is function of the preloading displacement, as follows:

$$\theta_{\text{in}} = \pm\sqrt{\frac{1}{\bar{H}(kL)}\frac{\Delta x}{L}} \tag{2}$$

where:

$$\begin{aligned}\bar{H}(kL) = \frac{kL}{8}[&\bar{A}^2(6kL - 8\sin(kL) + \sin(2kL)) \\ &+2\bar{A}\bar{B}(\cos(2kL) - 4\cos(kL) + 3) \\ &+\bar{B}^2(2kL - \sin(2kL))] + \frac{\bar{p}}{2}\end{aligned} \tag{3}$$

$$\bar{A} = -\frac{\cos(kL) - 1 - \bar{p}kL\sin(kL)}{kL(kL\sin(kL) + 2(\cos(kL) - 1))} \tag{4}$$

$$\bar{B} = -\frac{kL - \sin(kL) - kL\bar{p}(\cos(kL) - 1)}{kL(kL\sin(kL) + 2(\cos(kL) - 1))} \tag{5}$$

The ± sign in front of Eq. (2) indicates that the moment-angle characteristics of a fixed-lever buckled beam involve two symmetrical branches.

By varying the value of the product kL, the two branches of the parametric curve $(\theta_{\text{in}}, M_{\text{in,1beam}})$ are traced out in Figs. 2d and 2e for two arbitrary values of $\bar{p}$. The precompression displacement Δx is considered constant during the actuation. The

graphs are normalized to present a dimensionless, generalized representation of the actuation characteristics. When comparing Figs. 2d and 2e, we can observe that the lever length p has a direct impact on the moment-angle characteristics.

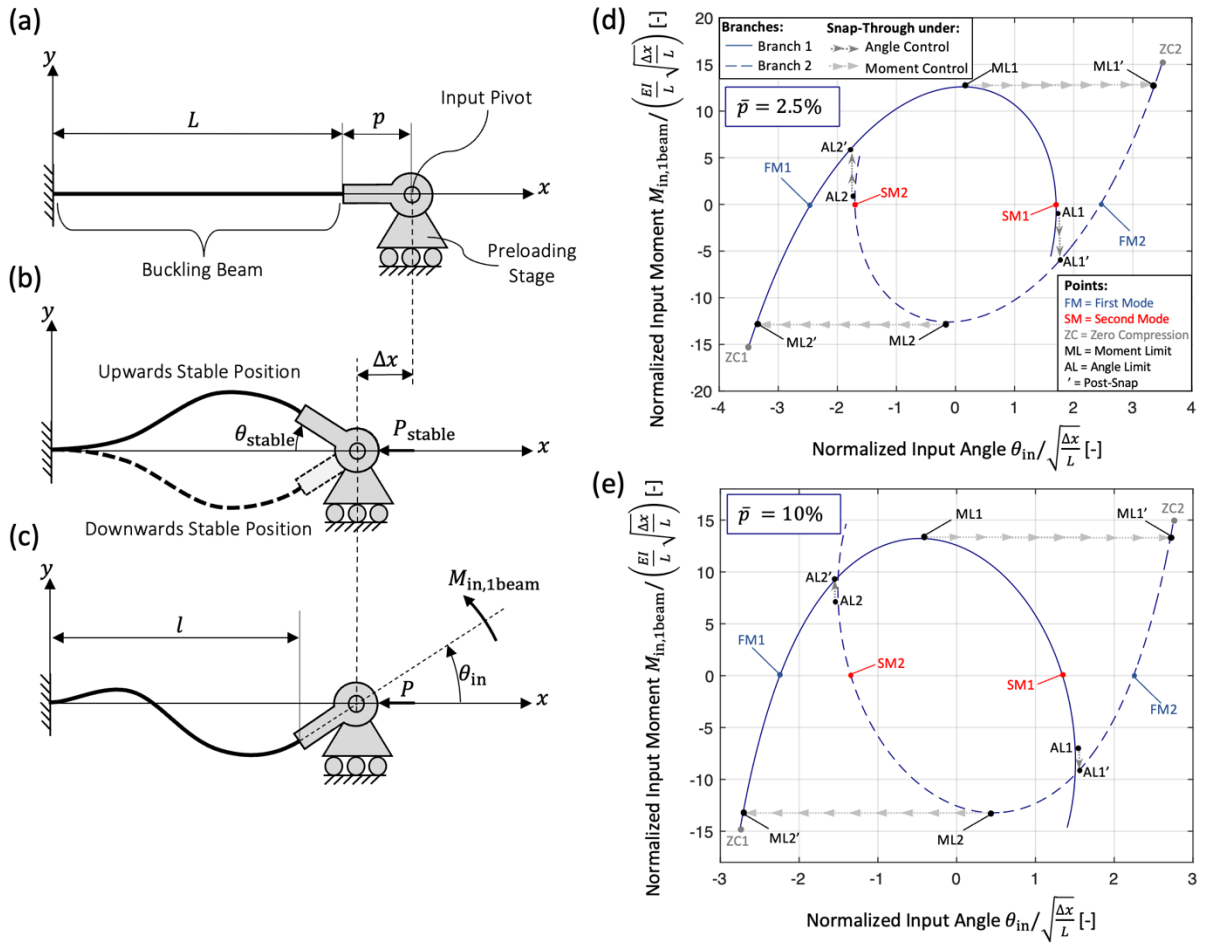

Figure 2. Fixed-lever buckled beam (a) as-fabricated, (b) buckled into one of its two stable positions, (c) when a moment is applied to the input pivot to switch between its two stable states, and (d-e) normalized actuation characteristics for two arbitrary lever length ratios $\bar{p} = 2.5\%$ and 10%, respectively.

3.1.2 Buckling modes and limit points

The buckling modes of the buckled beam are obtained by definition when the input moment $M_{\text{in,1beam}}$ is null. Substituting the constraint $M_{\text{in,1beam}} = 0$ in Eq. (1) results in a transcendental equation that does not have closed-form solutions and is a function of p. Therefore, numerical analysis is performed to obtain the first and second buckling modes, corresponding to the solutions where kL has the lowest values. The first buckling mode corresponds to the two stable deflections of the buckled beam with angle magnitude θ_{stable} (see Fig. 2b). The second buckling mode corresponds to unstable states, as do all higher-order buckling modes. The corresponding points are illustrated in the graphs of Figs. 2d and 2e, labelled FM1 and FM2, and SM1 and SM2 for the first and second buckling modes, respectively. Buckling modes beyond the

second are not illustrated, as moment and angle limit points are reached before these modes can be attained.

The buckled beam exhibits snap-through under angle control at limit points AL1 and AL2, see Fig. 2. After snap-through, the beam deflection corresponds to the points AL1' and AL2'. The buckled beam exhibits snap-through under moment control at limit points ML1 and ML2, see Fig. 2. After snap-through, the beam deflection corresponds to the points ML1' and ML2'. Zero compression points (labeled ZC1 and ZC2) are obtained when $kL = 0$ and correspond to the state of the beam when the axial load P is null. The tensile state of the beam (i.e., when $P < 0$) is not treated in this paper, as this state would result in a configuration where the internal stress in the beam becomes very high.

Remark 1: The second buckling mode corresponds to unstable positions that can lead to snap-through if the actuation does not allow the input moment to reverse sign. This occurs in some of the experiments in Sec. 5.2, where actuation is performed using an actuating pusher that cannot apply a negative input moment.

Remark 2: On the contrary to a fixed-pinned buckled beam (where $p = 0$), the second mode points SM1 and SM2 of a fixed-lever buckled beam can be reached before their respective angle limit points AL1 and AL2 (Tissot-Daguette et al., 2022b).

3.2 Pivot preloaded by two fixed-lever buckled beams

3.2.1 Actuation characteristics

In this section, we verify the assumption that connecting two fixed-lever buckled beams with symmetric buckling (i.e., having opposite buckling direction and equal precompression displacement Δx) to a pivot (as shown in Figs. 1a to 1c) allows to provide a negative angular stiffness which is relatively constant in the vicinity of the neutral position.

The input moment $M_{\text{in,2beams}}$ of the mechanism can be computed as the sum of the reaction moments $M_{\text{in,1beam}}$ of the two buckled beams operating angularly with opposite directions:

$$M_{\text{in,2beams}}(\theta_{\text{in}}) = M_{\text{in,1beam}}(\theta_{\text{in}}) - M_{\text{in,1beam}}(-\theta_{\text{in}}) \tag{6}$$

Equation (6) is difficult to solve analytically, because the reaction moments of the buckled beams do not share the same value for kL, except at the neutral position. To address this, a 20th-order polynomial expansion of $M_{\text{in,1beam}}(\theta_{\text{in}})$ is applied to compute Eq. (6) numerically. The absence of over- and underfitting is verified. Since snap-through occurs under angle control at $\theta_{\text{in}} = \pm\theta_{\text{in,lim}}$ (where $\theta_{\text{in,lim}}$ is the angle

magnitude at the limit points AL1 and AL2), θ_{in} restricted to the interval $[-\theta_{\text{in,lim}}, \theta_{\text{in,lim}}]$ when fitting $M_{\text{in,1beam}}$. The value of $\theta_{\text{in,lim}}$ is determined numerically by identifying the first local maximum of $\theta_{\text{in}}(kL)$ (Eq. (2)) as kL increases from 0.

Figure 3a shows $M_{\text{in,2beams}}$ as a function θ_{in} for different values of $\bar{p}$. For clarity, the corresponding branches 1 and 2 of $M_{\text{in,1beam}}$ (from Eq. (1) and (2)) are also plotted. It can be observed that the stiffness $K_{\text{in,2beams}} = M_{\text{in,2beams}}/\theta_{\text{in}}$ is nearly constant near the neutral position when two fixed-lever buckled beams are assembled in parallel with symmetric buckling directions. Moreover, this angular stiffness can be tuned by adjusting the lever length ratio $\bar{p}$. Notably, for high values of $\bar{p}$, $K_{\text{in,2beams}}$ becomes negative. This behavior can then be exploited to reduce the positive stiffness of a flexure pivot, such as an RCC pivot, as illustrated in Figs. 1d to 1f.

3.2.2 Axial load of the buckling beams

Since the stiffness of a flexure pivot can be affected by an applied radial force (Merriam et al., 2016; Zhao and Bi, 2010), the load P_0 exerted by the buckling beams on the pivot must be considered (see Fig. 1f). Depending on the orientation of the buckling beams, P_0 can correspond to either the sum or the difference of their axial forces $P = EI(kL)^2/L^2$. To illustrate this, Fig. 3b shows the two branches of the axial load P for a fixed-lever buckled beam with an arbitrary lever length $\bar{p} = 10\%$ as a function of θ_{in}. Two examples of buckling beam orientation are considered in Secs. 4.2 and 4.3, respectively.

3.2.3 Rotational stiffness

The stiffness constant $K_{\text{in,2beams,0}}$ is defined as the slope of the moment-angle characteristics $M_{\text{in,2beams}}(\theta_{\text{in}})$ at the neutral position. Analytically, $K_{\text{in,2beams,0}}$ is the sum of the tangential stiffness of the two buckled beams, which are equal at $\theta_{\text{in}} = 0$:

$$K_{\text{in,2beams,0}} = 2\frac{dM_{\text{in,1beam}}}{d\theta_{\text{in}}}(\theta_{\text{in}} = 0) \tag{7}$$

Since $M_{\text{in,1beam}} = K_{\text{in,1beam}}\theta_{\text{in}}$ and θ_{in} are both functions of kL (see Eqs. (1) and (2)), we apply the chain rule to calculate $K_{\text{in,2beams,0}}$. Noting that $kL = 2\pi$ when $\theta_{\text{in}} = 0$, Eq. (7) can be expressed as:

$$K_{\text{in,2beams,0}} = 2\lim_{kL\to 2\pi}\left(\frac{\frac{dK_{\text{in,1beam}}}{d(kL)}\theta_{\text{in}}}{\frac{d\theta_{\text{in}}}{d(kL)}} + K_{\text{in,1beam}}\right) = \frac{EI}{L}\left(3 - 8\pi^2(\bar{p} + \bar{p}^2)\right) \tag{8}$$

From Eq. (8), the stiffness constant $K_{\text{in,2beams,0}}$ is positive if $\bar{p} < 3.67\%$, and negative otherwise. In that case, the pivot in Figs. 1a to 1c can either be monostable or bistable,

depending on the selected value of $\bar{p}$. We plot $K_{\text{in,2beams,0}}$ as a function of $\bar{p}$ in Fig. 3c to help designers in selecting the value of $\bar{p}$ for their application. Note that the incorporation of two fixed-pinned buckled beams in a flexure pivot cannot provide a stiffness reduction (see Fig. 3c where $\bar{p} = 0$).

Remark 3: Interestingly, as $\bar{p}$ tends to infinity, the mechanism approaches a linear stage preloaded by two fixed-guided buckled beams. The analytical formulas derived in this paper can thus be applied to model such a structure by converting the moment into a force ($F_{\text{in}} = M_{\text{in}}/p$) and the angle into a translation displacement ($d_{\text{in}} = \theta_{\text{in}} p$). In this case, the stable angles would then correspond to the stable translational positions of the linear stage. The two angle limit points, AL1 and AL2, would become bifurcation points, as the two branches yield identical characteristics between these points. Indeed, the stiffness is negative and constant in this region (Dijksman, 1979). From Eq. (8), the stiffness constant of the two fixed-guided buckled beam can be calculated as $F_{\text{in}}/d_{\text{in}} = -8\pi^2 EI/L^3$, in agreement with (Dijksman, 1979).

If the pivot is implemented with flexures (Figs. 1d to 1f), the overall angular stiffness is simply the sum of the stiffness $K_{\text{in,guide}}$ of the guiding beams and the stiffness $K_{\text{in,2beams}}$ applied by the two buckled beams:

$$K_{\text{in,tot}} = K_{\text{in,guide}} + K_{\text{in,2beams}} \tag{9}$$

Note that $K_{\text{in,guide}}$ can be a function of the radial load P_0 applied by the buckling beams to the guiding beams (Sec. 3.2.2). Depending on the value of $K_{\text{in,tot}}$, the pivot can either be monostable (positive stiffness), statically balanced (near-zero stiffness), or bistable (negative stiffness).

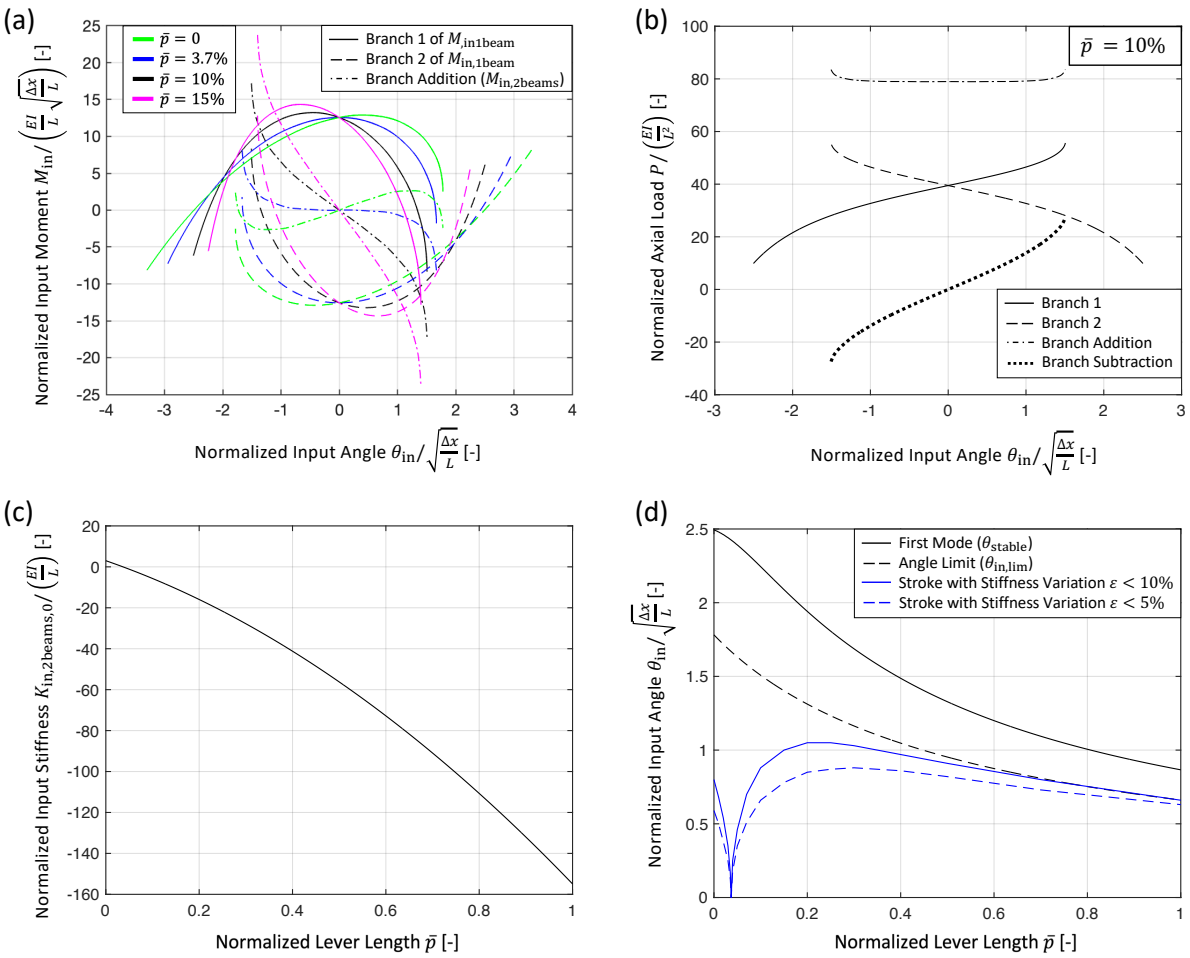

Figure 3. Normalized actuation characteristics of a pivot preloaded by two fixed-lever buckled beams (mechanism shown in Figs. 1a to 1c). (a) Moment-angle branches of each fixed-lever buckled beam ($M_{\text{in,1beam}}(\theta_{\text{in}})$) and the total moment ($M_{\text{in,2beams}}(\theta_{\text{in}})$) applied to the pivot for various lever length ratios $\bar{p}$. (b) Branches of the axial load with respect to the input angle applied by each fixed-lever buckled beam, and branch addition and subtraction. (c) Angular stiffness constant of the pivot as a function of the lever length ratio. (d) Critical input angle magnitudes: first mode, angle limit and maximum angular displacements where the variation of the secant stiffness from the stiffness constant remains lower than 5% and 10%.

3.2.4 Angular stroke

In case it is desired for the actuation characteristics to remain in a nearly constant stiffness region, the pivot stroke is limited by the angle limit points of the fixed-lever buckled beams. Indeed, the buckled beams should not snap under angle control, otherwise they would be placed in antisymmetric buckling where the moment-angle characteristics are highly nonlinear. If such snapping occurs, one of the beams must be manually reset to restore symmetric buckling.

The angle limit magnitude $\theta_{\text{in,lim}}$ is provided in Fig. 3d with respect to the normalized lever length $\bar{p}$. The stable angle magnitude θ_{stable} is also plotted in this figure for comparison purposes. We can see that both θ_{stable} and $\theta_{\text{in,lim}}$ decrease when increasing the lever length ratio. From Figs. 3c and 3d, a compromise when adjusting the value of $\bar{p}$ can be noticed as it is difficult to have both a large angular stroke and an elevated

stiffness reduction. Figs. 3c and 3d highlight the trade-off in choosing $\bar{p}$, as achieving both a large angular stroke and a significant stiffness reduction is challenging.

Certain applications require specific linearity in the moment-angle characteristics, which further limits the operating rotation amplitude. The variation of the stiffness relative to the stiffness constant can be normalized as follows:

$$\varepsilon(\theta_{\text{in}}) = \frac{K_{\text{in,2beams}}(\theta_{\text{in}}) - K_{\text{in,2beams,0}}}{K_{\text{in,2beams,0}}} \tag{10}$$

This serves as a way to evaluate the nonlinearity of the moment-angle characteristics. In Fig. 3d, we plot the maximum range of θ_{in} where $\varepsilon < 5\%$ and $\varepsilon < 10\%$. We can see that the stroke for $\varepsilon < 5\%$ and $\varepsilon < 10\%$ is maximum if $\bar{p} \cong 20\%$. Note that the stiffness nonlinearity of the flexure pivot itself should also be considered when computing the total stiffness variation. This would typically be important for horological applications (Thalmann et al., 2020). In Sec. 4, we neglect the nonlinearity of the flexure pivots for simplification reasons.

The angular stroke of the pivot is also constrained by the admissible stress σ_{adm} of the material, which may be based on either the yield strength or the fatigue strength, depending on the application. To ensure that the maximum stress σ_{max} in the buckling beam does not exceed σ_{adm}, we compute σ_{max} as the sum of the axial compression $P/(bh)$ and the bending stress (Tissot-Daguette et al., 2022b) and, as follows:

$$\sigma_{\text{max}} = \frac{Eh^2}{12L^2}(kL)^2 + \frac{Eh}{2L^2}(kL)^2 \max\left(\left|A\sin\left(kL\frac{s}{l}\right) + B\cos\left(kL\frac{s}{l}\right)\right|\right), \quad \text{with } s \in [0, L] \tag{11}$$

where E stands for the material Young's modulus, h is the beam thickness, b is the beam width, and $A = \bar{A}L\theta_{\text{in}}$ and $B = \bar{B}L\theta_{\text{in}}$ are deflection parameters given by Eqs. (4) and (5).

4 Mechanism design and manufacturing

Prototypes of the mechanisms presented in Secs. 2 and 3 are designed and fabricated to experimentally validate the analytical modeling in Sec. 3 as well as to demonstrate the suitability of using fixed-lever buckled beams in the design of a near-zero stiffness pivot. To this end, three mechanisms are designed:

1. Single fixed-lever buckled beam
2. Cross-spring pivot preloaded by two fixed-lever buckled beams
3. RCC pivot preloaded by two fixed-lever buckled beams

These mechanisms are presented in Secs. 4.1 to 4.3, respectively.

4.1 Single fixed-lever buckled beam

The single fixed-lever buckled beam is made out of a metal strip (spring steel 1.1274 from Brütsch/Rüegger Tools Ltd) with a thickness $h = 0.2$ mm, a width $b = 25$ mm and an effective length $L = 200$ mm. This mechanism is meant to experimentally verify the analytical moment-angle characteristics presented in Sec. 3.1. Young's modulus E and yield strength σ_y of the material and the selected dimensions are listed in Table 1. We consider two arbitrary lever length ratios ($\bar{p} = 2.5\%$ and $\bar{p} = 10\%$) to compare the results.

Table 1. Design parameters of the single fixed-lever buckled beam.

	Parameter	Value
Material (spring steel 1.1274)	E	210 GPa
	σ_y	1600 MPa
Beam dimensions	h	0.2 mm
	b	25 mm
	L	200 mm
	p	5 mm / 20 mm
Precompression	Δl	2 mm 4 mm

4.2 Cross-spring pivot preloaded by two fixed-lever buckled beams

The second mechanism considers the case where the flexure pivot in Figs. 1d to 1f is replaced by a cross-spring pivot. The resulting monolithic, planar structure is shown in Fig. 4. The guiding beams cross at the midpoint of their lengths. In the neutral position, the buckling beams are orientated so that their longitudinal axes are concurrent on the crossing axis of the guiding beams (which corresponds to the instantaneous center of rotation). The cross-spring pivot is oriented such that its parasitic shift λ_0, which is primarily along the bisector of the guiding beam axis (Zhao and Bi, 2010), is perpendicular to the longitudinal axis of the buckling beams (see Figs. 4d to 4e). Since the radial load P_0 applied by the two buckling beams is perpendicular to the pivot parasitic shift, we consider that the angular stiffness of the whole structure is not modified by this load. The total angular stiffness is then given by Eq. (9) where the flexure pivot stiffness is simply $K_{\text{in,guide}} = 8EI/L$ (Cosandier et al., 2017).

The mechanism is fabricated with a fused filament 3D printer (Bambu Lab A1). The filament is made of polycarbonate (PC FR from Bambu Lab). This material was chosen over conventional PolyLactic Acid (PLA) filament to reduce structure creep (Dogan, 2022). A nozzle diameter of 0.2 mm was employed. The bed and nozzle temperatures were set to 100°C and 260°C, respectively. The thickness $h = 0.3$ mm of all the beams was measured with a caliper. The out-of-plane thickness of the mechanism is $b = 5$

mm. The other dimensions and material parameters are shown in Table 2. Preloading screws and fixed nuts are integrated in the structure to preload the buckling beams to specific precompression displacements Δx.

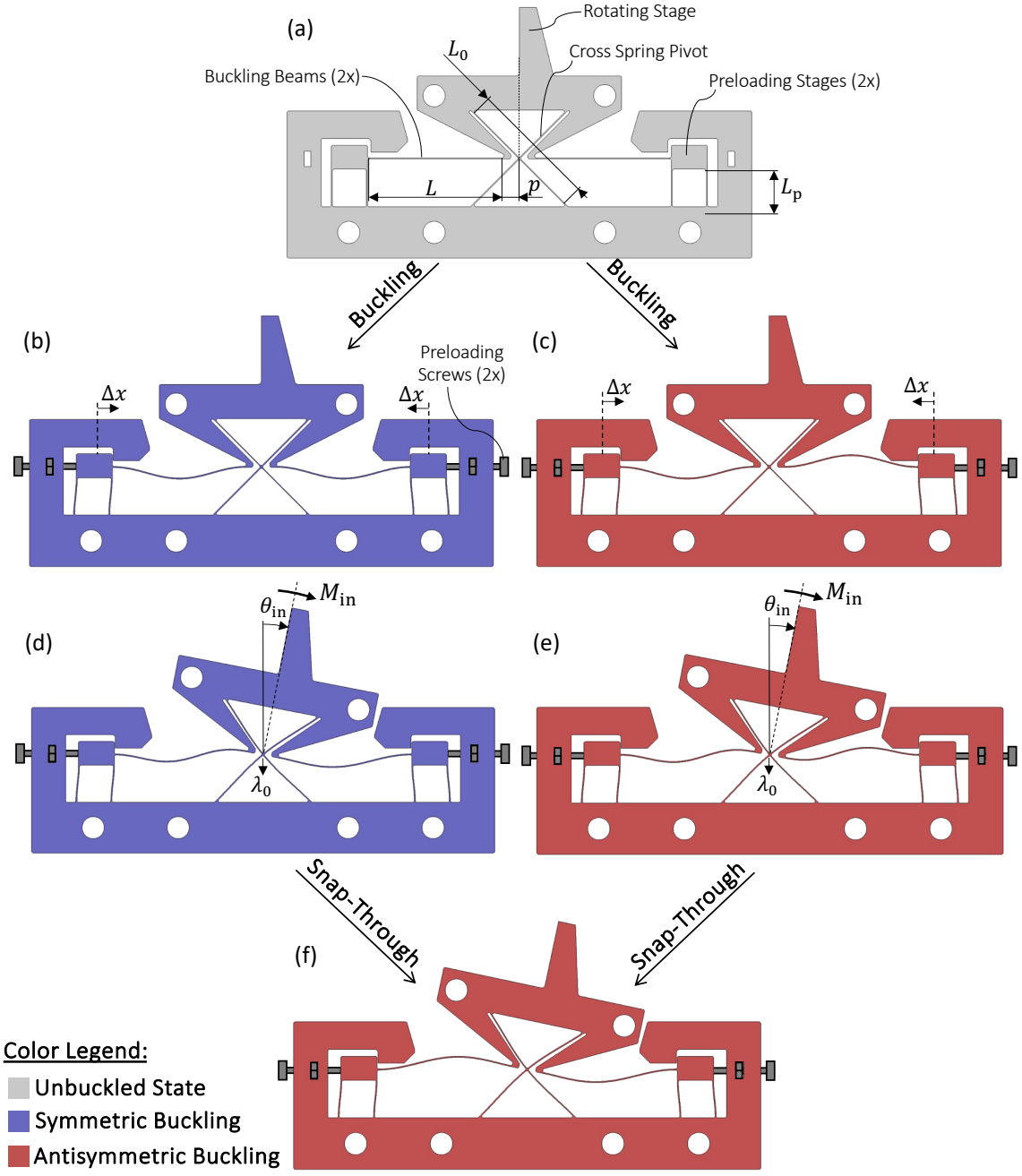

Figure 4. Cross-spring pivot preloaded by two horizontal fixed-lever buckled beams (a) as-fabricated, (b) in neutral position where the horizontal beams have buckled in a symmetric buckling configuration, (c) in neutral position where the horizontal beams have buckled in an antisymmetric buckling configuration, (d-e) mechanisms in (b) and (c) in angle limit position, i.e., just before snap-through, and (f) position just after snap-through.

Note that only a single set of dimensions and a single precompression displacement Δx are considered. Nevertheless, both configurations of the symmetric and antisymmetric buckling beams will be tested (see Fig. 4). It should be noted that if the beams buckle

in the antisymmetric configuration, the mechanism cannot return to the symmetric configuration without manually reversing the buckling direction of one of the beams.

Remark 4: The symmetric buckling configuration is illustrated in Figs. 4b and 4d in the case where the two horizontal beams buckled downwards. However, we need to mention that the opposite (where they buckle upwards) would result in the same actuation characteristics.

Table 2. Design parameters of the 3D-printed polycarbonate cross-spring pivot.

	Parameter	Value
Material (Bambu PC FR)	E	1700 MPa
	σ_y	50 MPa
Guiding beams	L_0	35 mm
Buckled beams	L	40 mm
	p	4.5 mm
Preloading stage	L_p	10 mm
Precompression	Δx	0.75 mm

4.3 RCC pivot preloaded by two fixed-lever buckled beams

To verify the concept at the microscale, we test silicon prototypes of an RCC pivot preloaded by two fixed-lever buckling beams. Rather than relying on geometric preloading with position-adjustable linear stages (which is challenging at the microscale), we preload the buckling beams using thin film residual stress (Despont et al., 2020). We integrate Preloading Chevron Mechanism (PCM) that uses thermal oxidation of silicon to preload the pivot mechanism without post-fabrication actions (Tissot-Daguette et al., 2025).

Since the preloading stages must have identical preloads to avoid a moment offset in the moment-angle characteristics, we decided to combine the two preloading stages (see Fig. 1) into a single stage and place it on the opposite side from the RCC pivot. Due to manufacturing constraints, the buckling beams are set parallel. The parameter r denotes the off-center distance between the longitudinal axis of a buckling beam and the rotation center of the pivot in neutral position (see Fig. 5).

The fabrication of the prototypes starts with a Deep Reactive Ion Etching (DRIE) process performed on a monocrystalline (100)-oriented p-type silicon wafer. A silicon dioxide layer is subsequently grown on the etched wafer by wet thermal oxidation at 1050°C under atmospheric pressure. The wafer is then cooled to room temperature, generating thermal stresses in the oxide layer due to the mismatch in the coefficients of thermal expansion of silicon and silicon dioxide. The resulting residual stress,

consisting of both intrinsic and thermal stress components, is exploited to buckle the buckling beams, thereby reducing the angular stiffness of the RCC pivots.

All the beams are designed with equal cross-section. The thickness of the silicon core is $h_s = 20$ µm and the out-of-plane depth (which corresponds to the wafer thickness) is $b_s = 380$ µm. The thickness of the silicon dioxide film (grown all around the silicon core) is $h_f = 3$ µm. The PCM is composed of 62 preloading beams. The design methodology given in (Tissot-Daguette et al., 2025) is employed to design the length L_p and the inclination α of the preloading beams of the PCM. Three values for the buckling beam length L (see Table 3) are selected to capture different levels of stiffness reduction. A prototype without buckling beams is also manufactured and tested to evaluate the stiffness reduction.

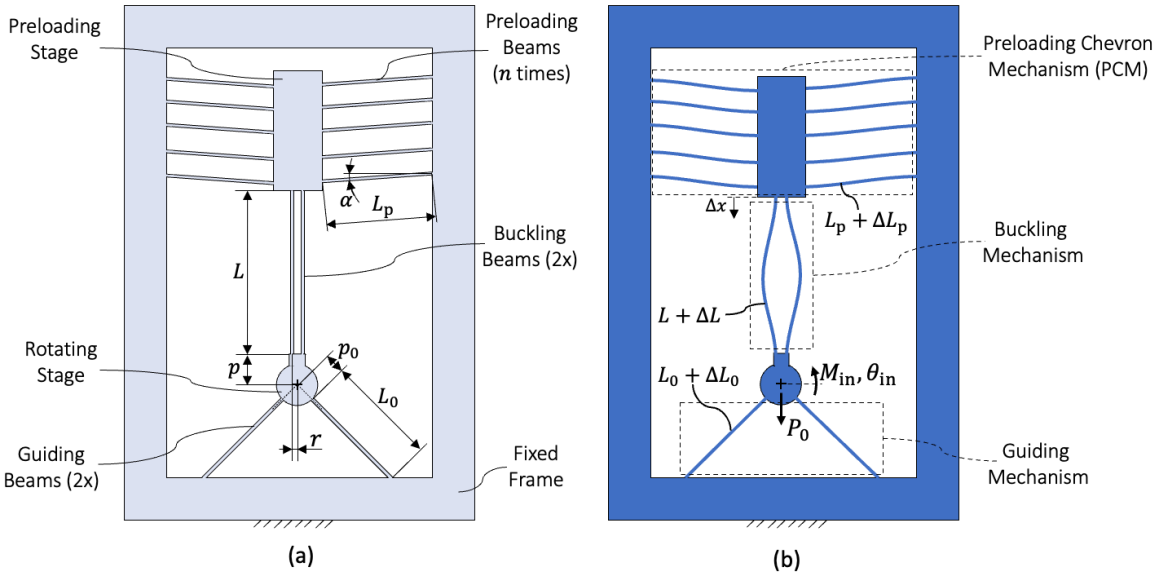

Figure 5. RCC pivot preloaded by two vertical fixed-lever buckled beams in neutral position (a) before and (b) after residual stress is applied (resulting in an increase in length of all the beams).

Table 3. Design parameters of the silicon RCC pivots.

	Parameter	Value
Materials (silicon and oxide film)	$E_{s,100}$	130 GPa
	$E_{s,110}$	165 GPa
	E_f	75 GPa
	σ_y	800 MPa
Guiding beams	L_0	2.95 mm
	p_0	0.05 mm
Buckling beams	L	4.5 mm / 4.75 mm / 4.85 mm
	p	0.3 mm
Preloading Chevron Mechanism (PCM)	L_p	3 mm
	α	1.3 deg

As opposed to the cross-spring pivot presented in Sec. 4.2, the parasitic shift of the RCC pivot is aligned with the radial force P_0 applied by the buckling beams. This preload must be considered when computing the angular stiffness. As the radial force is the sum of the axial loads of the left and right buckling beams (i.e., $P_0 = P_{\text{left}} + P_{\text{right}}$), it corresponds to the addition of the two branches of the axial load P. The branch addition being nearly constant with respect to θ_{in} (see Fig. 3b), P_0 is approximated by two times the axial load P obtained in neutral position (i.e., when $kL = 2\pi$), as follows:

$$P_0 \cong \frac{8\pi^2 (EI)_{\text{tot},100}}{L^2} \tag{12}$$

where $(EI)_{\text{tot},100} = E_{\text{f}} I_{\text{f}} + E_{\text{s},100} I_{\text{s}}$ is the equivalent flexural modulus of the beams, with $I_{\text{f}} = b_{\text{s}}((h_{\text{s}} + 2h_{\text{f}})^3 - h_{\text{s}}^3)/12$ and $I_{\text{s}} = b_{\text{s}} h_{\text{s}}^3/12$ the quadratic moments of the film and substrate, respectively. Since the buckling beams are aligned with the <100> direction of the silicon crystal, Young's modulus in this orientation is given by $E_{\text{s},100} = 130$ GPa. The oxide Young's modulus is assumed to be isotropic and equal to $E_{\text{f}} = 75$ GPa.

Since the axial load P in the two buckling beams varies differently when the input pivot is rotated (see the branch subtraction curve in Fig. 3b), the distance r applies an additional moment $M_r = (P_{\text{left}} - P_{\text{right}}) \cdot r$ to the pivot. This adds a stiffness constant $K_{\text{in},r}$ to the mechanism's total angular stiffness. Since the branch subtraction is approximately linear with respect to θ_{in}, $K_{\text{in},r}$ can be computed by differentiating P with respect to θ_{in} at $\theta_{\text{in}} = 0$. Using Eq. (2) and applying the chain rule leads to:

$$\begin{aligned} K_{\text{in},r} = \lim_{\theta_{\text{in}} \to 0} \left(\frac{dM_r}{d\theta_{\text{in}}} \right) = 2r \lim_{\theta_{\text{in}} \to 0} \left(\frac{dP}{d\theta_{\text{in}}} \right) = 2r \lim_{kL \to 2\pi} \left(\frac{\frac{dP}{d(kL)}}{\frac{d\theta_{\text{in}}}{d(kL)}} \right) \\ = \frac{4\pi r (EI)_{\text{tot},100}}{L^2 \sqrt{\frac{\Delta x}{L}}} \end{aligned} \tag{13}$$

Remark 5: In this analytical model, the precompression displacement of the buckling beams Δx is approximated as the preloading displacement provided by the PCM (see Fig. 5). In other words, we neglect the variations of length ΔL and ΔL_0, and only consider ΔL_{p} to compute Δx. The deflection of the PCM is computed using the same method as described in (Tissot-Daguette et al., 2025).

When the mechanism is non-preloaded (i.e., in the absence of buckling beams), the input stiffness corresponds to that of an RCC pivot, as given by (Cosandier et al., 2017):

$$K_{\text{in,guide},0} = K_{\text{in,guide}}(P_0 = 0) = \frac{8(EI)_{\text{tot},110}\left(1 + 3\overline{\text{p}_0} + 3\overline{\text{p}_0}^2\right)}{L_0} \tag{14}$$

where $\overline{p_0} = p_0/L_0$, and $(EI)_{\text{tot},110} = E_{\text{f}} I_{\text{f}} + E_{\text{s},110} I_{\text{s}}$. We use the silicon Young's modulus $E_{\text{s},110} = 169$ GPa, because the guiding beams are aligned with the <110> silicon crystallographic direction.

When the mechanism is preloaded by the two fixed-lever buckled beams, the total angular stiffness given by Eq. (9) becomes:

$$K_{\text{in,tot}} = K_{\text{in,guide}}(P_0) + K_{\text{in,2beams}} + K_{\text{in},r} \tag{15}$$

Since the guiding beams have the same type boundary conditions as the buckling beams (i.e., fixed-lever), the flexure pivot stiffness $K_{\text{in,guide}}(P_0)$ can be computed using Eq. (1), as follows:

$$K_{\text{in,guide}}(P_0) = \\ = 2\frac{(EI)_{\text{tot},110}}{L_0} k_0 L_0 \frac{k_0 L_0 \cos(k_0 L_0) - \sin(k_0 L_0)\left(1 + (k_0 L_0)^2 \overline{p_0} + (k_0 L_0)^2 \overline{p_0}^2\right)}{k_0 L_0 \sin(k_0 L_0) + 2(\cos(k_0 L_0) - 1)} \tag{16}$$

where the compression parameter $k_0 = \sqrt{(P_0/\sqrt{2})/(EI)_{\text{tot},110}}$, the guiding beams being oriented at 45 deg with respect to the preload P_0.

Mechanical stops are used to ensure that the magnitude of the input angle θ_{in} remains below the angle limit $\theta_{\text{in,lim}}$. Exceeding this limit would cause the mechanism to irreversibly snap into the antisymmetric buckling configuration. Returning to the symmetric configuration would require manually reversing the buckling direction of one beam, which is extremely challenging given the very close spacing of the beams, with a neutral-axis separation of only 50 µm. To ensure outward buckling directions after the thermal oxidation process, the beams are initially precurved with a centroid offset of 2 µm.

Figure 6 shows photographs of preloaded RCC pivot prototypes. The prototypes with buckling beam lengths $L = 4.75$ mm and $L = 4.85$ mm exhibit monostable behavior, whereas the prototype with $L = 4.5$ mm is bistable, as illustrated in Fig. 6b, where the rotating stage is in contact with one of the two mechanical stops.

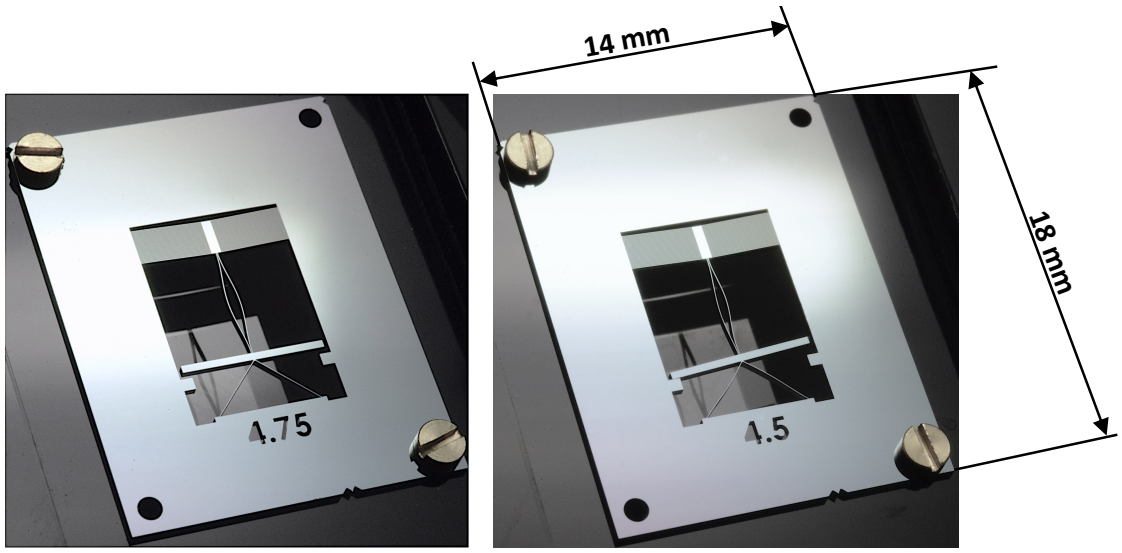

Figure 6. Photographs of preloaded RCC pivot silicon prototypes (a) with a buckling beam length of $L = 4.75$ mm (monostable) and (b) of $L = 4.5$ mm (bistable). Parts manufactured by CSEM (Centre Suisse d'Electronique et de Microtechnique) in 2024.

5 Model validation

5.1 FEM simulations

In order to verify the stiffness characteristics of the three mechanisms designed in Sec. 4, FEM studies were conducted using the commercial software COMSOL Multiphysics 6.1. Since all the mechanisms are planar, the 2D simulations were performed with plane stress approximation. The stationary solver uses the Solid Mechanics module and the Geometric Nonlinearity setting to capture large deformation, buckling, and snap-through behaviors. A segregated solver approach was used to improve convergence. All mechanisms were simulated using the dimensions and materials specified in Tables 1 to 3.

For each mechanism, the simulation was divided into two successive sub-studies:

- Study 1: A lateral force of 0.5 N was applied to the side of the buckling beams to force their buckling in a desired direction. This study was conducted to accelerate solver convergence and avoid unrealistic buckling modes.
- Study 2: Reusing the solution of Study 1 and removing the lateral force, the rotational stiffness of the mechanisms was obtained by varying the angular position θ_{in} of a rigid connector attached to the rotating stage and evaluating the reaction moment M_{in}. For each mechanism, the von Mises stress was verified to be less than the estimated yield strength σ_y of the different materials given in Tables 1 to 3.

The single fixed-lever buckled beam was meshed with quadrilateral shell elements such that four elements are mapped across the beam thickness h and one element every 50 µm along the length L. Note that the lever was not meshed, as it is assumed to be infinitely rigid in the simulations.

For the preloaded cross-spring pivot mechanism, all the beams were meshed with quadrilateral shell elements such that four elements are mapped across their thickness, and one element every 200 µm along their length. The rest of the structure is meshed with free triangular elements.

For the preloaded RCC pivot silicon mechanisms, all the beams were meshed with quadrilateral shell elements such that four elements are mapped across the silicon thickness h_s, one element for the oxide thickness h_f (on both sides of the beam thickness), and one element every 20 µm along their length. The rest of the structure is meshed with free triangular elements. A biaxial residual stress of -290 MPa (compressive) was applied in the buckling and preloading beams using the same FEM method as in (Tissot-Daguette et al., 2025). Since it is known that the fixed frame stiffness can impact the actuation characteristics of PCM-based silicon mechanisms, the silicon preloaded RCC pivot mechanisms were simulated with either a fixed frame considered infinitely rigid (Fig. 7a) or having the actual manufactured frame shape and with the elastic parameters of silicon (Fig. 7b).

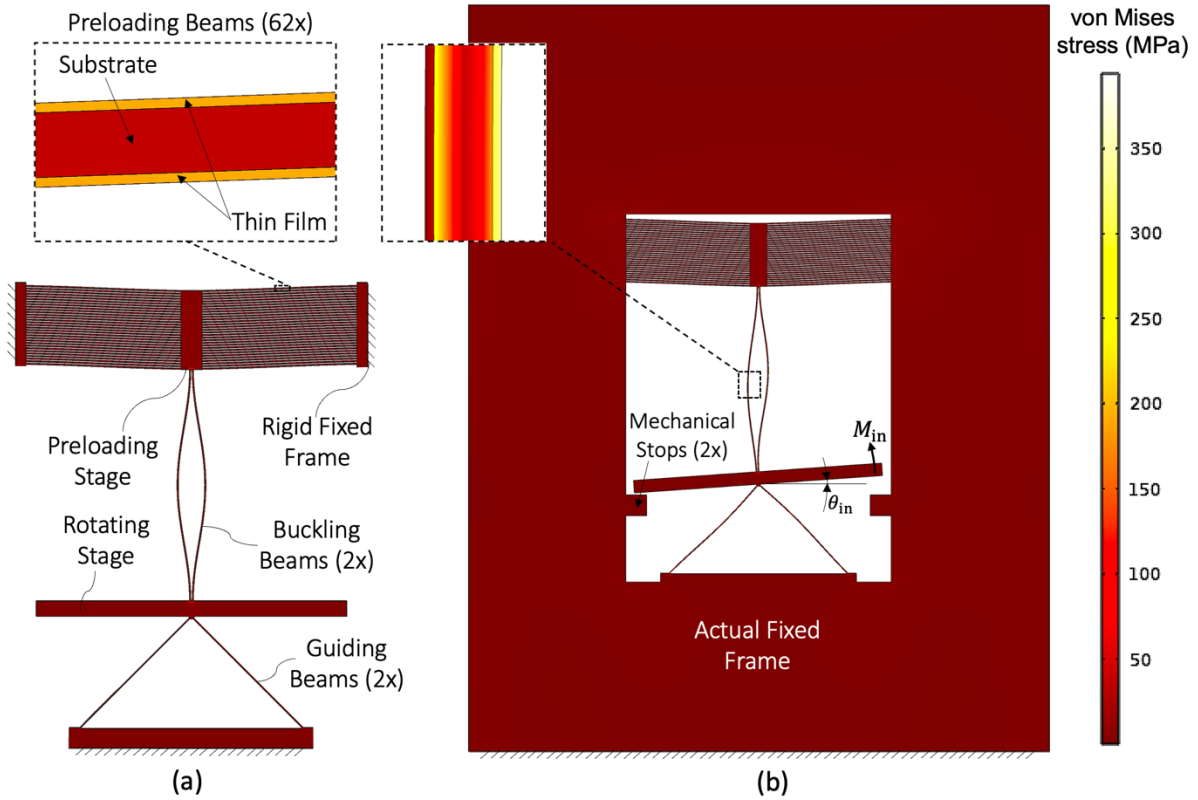

Figure 7. FEM simulation of the RCC pivot with a buckling beam length of $L = 4.5$ mm placed in neutral position, considering that the mechanism fixed frame is (a) fully rigid or (b) elastic (same material and dimensions as fabricated). Insets show the von Mises stress distribution at the beam center.

5.2 Experiments

The moment-angle characteristics of the three mechanisms were experimentally evaluated using dedicated test benches. Each setup employed a manual micro-positioning stage to apply the input angle θ_{in} and a force sensor to measure the corresponding input moment M_{in}. Prior to testing, the force sensor was calibrated to ensure accurate measurements. All tests were conducted in a horizontal plane with the system at static equilibrium to minimize gravity and dynamic effects. Measurements were repeated five times and averaged to reduce noise.

Figure 8 presents the test bench used to characterize the single fixed-lever buckled beam. The setup is similar to that presented in (Tissot-Daguette et al., 2022b), which was designed to measure the characteristics of pinned-pinned and fixed-pinned buckled beams. In the present work, the bench is adapted to accommodate a buckled beam with a fixed-lever support. The beam is attached to a rotating lever mounted on ball bearings at one end and clamped at the other. A force sensor (Kistler 9207 with force-introducing cap No. 3.220.139), mounted on linear stages, applies a lateral load through a slot in the lever. The distance between the rotation axis and the sensor cap contact point is 20 mm. An axial linear stage sets the precompression displacement Δx, while a lateral linear stage guides the force sensor to impose the input angle. The experiment starts when the beam is in a stable position and ends when snap-through has occurred. Because the force sensor can only push the rotating stage in one direction, the measured input moment was restricted to positive values. The measurement uncertainties are ± 1.3 deg for the input angle, ± 4 Nmm for the input moment, and ± 10 µm for the end-shortening.

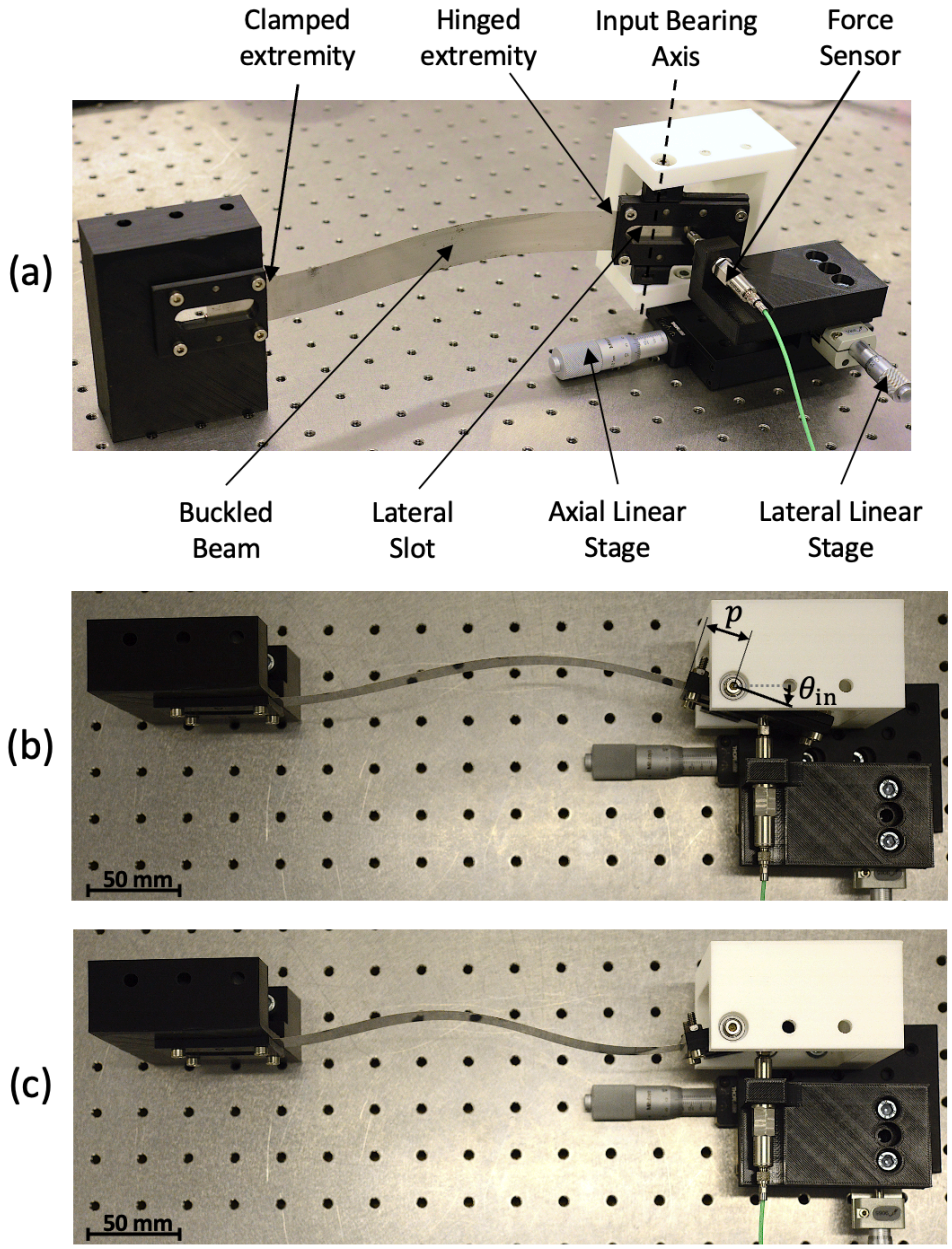

Figure 8. Test bench used to measure the moment-angle characteristics of a single fixed-lever buckled beam: (a) components of the test bench, (b) the buckled beam having a lever length $p = 20$ mm is shown in first mode (stable position) and (c) close to the second mode (unstable position).

For the preloaded cross-spring pivot, the test bench consists of an actuating pin (ø1 mm) mounted on a force sensor (Futek LPM200) itself mounted on a 3-axis manual translation stage, see Fig. 9. Because this force sensor is prone to deformations when loaded, a displacement sensor (Keyence LK-H082) is used to accurately measure the position of the actuating pin, thus the input angle. The distance between the rotation axis and the contact point of the actuating pin on the rotation stage is 38 mm. The experiment starts at a stable position and stops when snap-through occurs. The mechanism is tested under both symmetric and antisymmetric buckling configurations. Due to the setup, the measured input moment was restricted to positive values. The measurement uncertainties are $\pm 3 \times 10^{-3}$ deg for the input angle, $\pm 0.4 \times 10^{-3}$ Nmm for the input moment, and ± 25 μm for the precompression displacement.

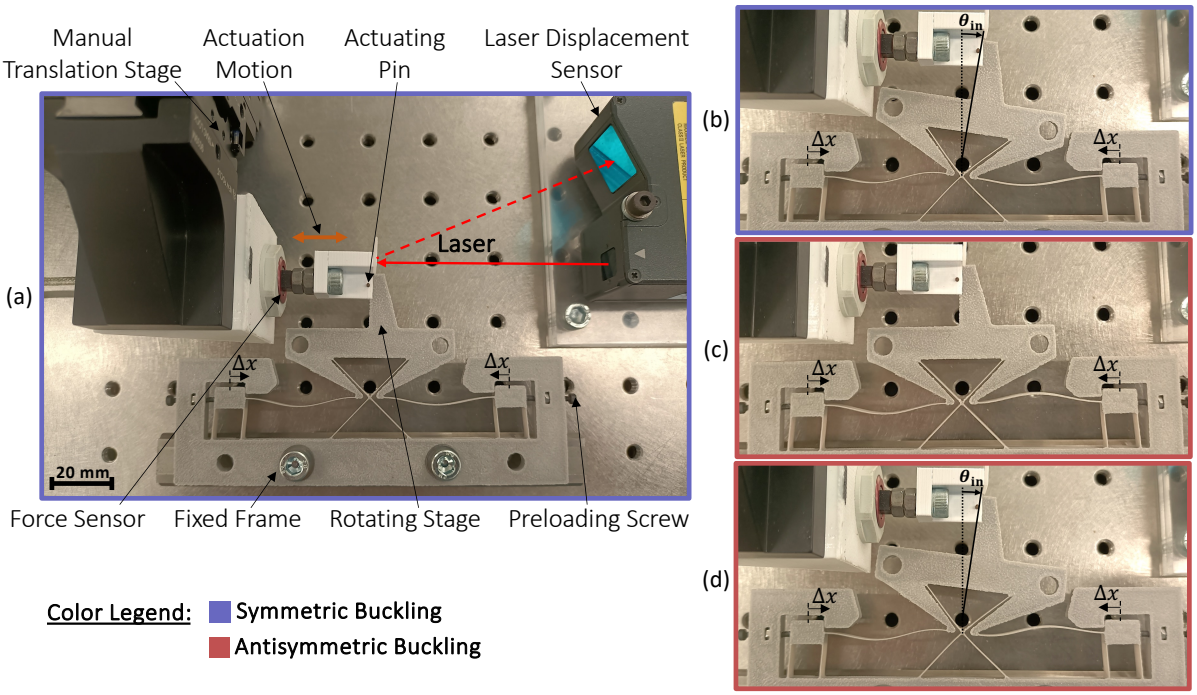

Figure 9. Test bench used to measure the moment-angle characteristics of the preloaded cross-spring pivot. The mechanism is shown (a) in symmetric buckling neutral position (stable equilibrium), (b) in symmetric buckling close to one of its two unstable positions (just before the left buckled beam snaps), (c) in antisymmetric buckling neutral position (not in equilibrium), and (d) in antisymmetric buckling close to one of its two unstable positions (just before the two buckled beams snap).

The preloaded RCC pivot was tested using the same bench employed for the preloaded cross-spring pivot (see Fig. 10). The distance between the rotation axis and the contact point of the actuating pin on the rotation stage is 2.5 mm. The experiment starts at the pivot's neutral position and stops when the rotating stage reaches one of the integrated end stops. By alternately pushing on both sides of the rotating stage, we were able to measure the input angle in both directions. The measurement uncertainties are $\pm 46 \times 10^{-3}$ deg for the input angle, $\pm 0.03 \times 10^{-3}$ Nmm for the input moment.

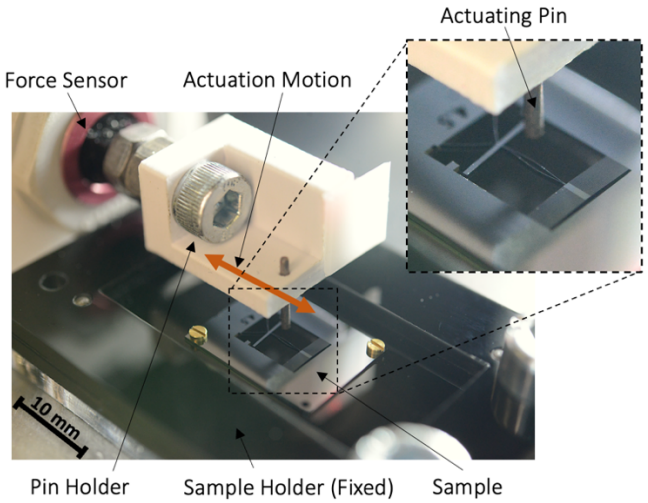

Figure 10. Preloaded RCC pivot silicon prototype mounted on the same test bench as shown in Fig. 9 for moment-angle characteristics measurement. The zoom inset shows how the actuating pin is placed in contact with the sample rotating stage for stiffness measurement.

6 Results and discussion

In this section, analytical, FEM and experimental results are presented together for the actuation characteristics of the three mechanisms that we have designed in Sec. 4. Possible discrepancies between the results allow to evaluate the accuracy of the analytical model presented in this paper.

6.1 Single buckled beam

Using Eqs. (1), (2) and (11), the input moment and maximum internal stress of the single fixed-lever buckled beam are plotted in Fig. 11 as functions of the input angle for the two selected lever lengths. The proposed model captures the essential actuation characteristics of the buckled beam, as the analytical predictions align well with the FEM results. Some discrepancies appear between the models and the measurements near the neutral position, with a maximum relative deviation of 8.2% for the input moment. These differences can be attributed to manufacturing and assembly tolerances, slight initial imperfections in the beam, and friction in the bearings.

The FEM results confirm that the beam snaps at the expected angle limit points. The magnitude of this limit angle can be tuned by adjusting the applied precompression. Comparing the two lever lengths (Figs. 11a and 11b) shows that the moment-angle characteristics change as predicted. In both cases, the internal stress increases from the stable position up to the corresponding angle limit point. The von Mises stress obtained from FEM remains below the material's yield strength. It is worth noting that if the magnitude of the input angle exceeds the stable angle, the internal stress would rise sharply.

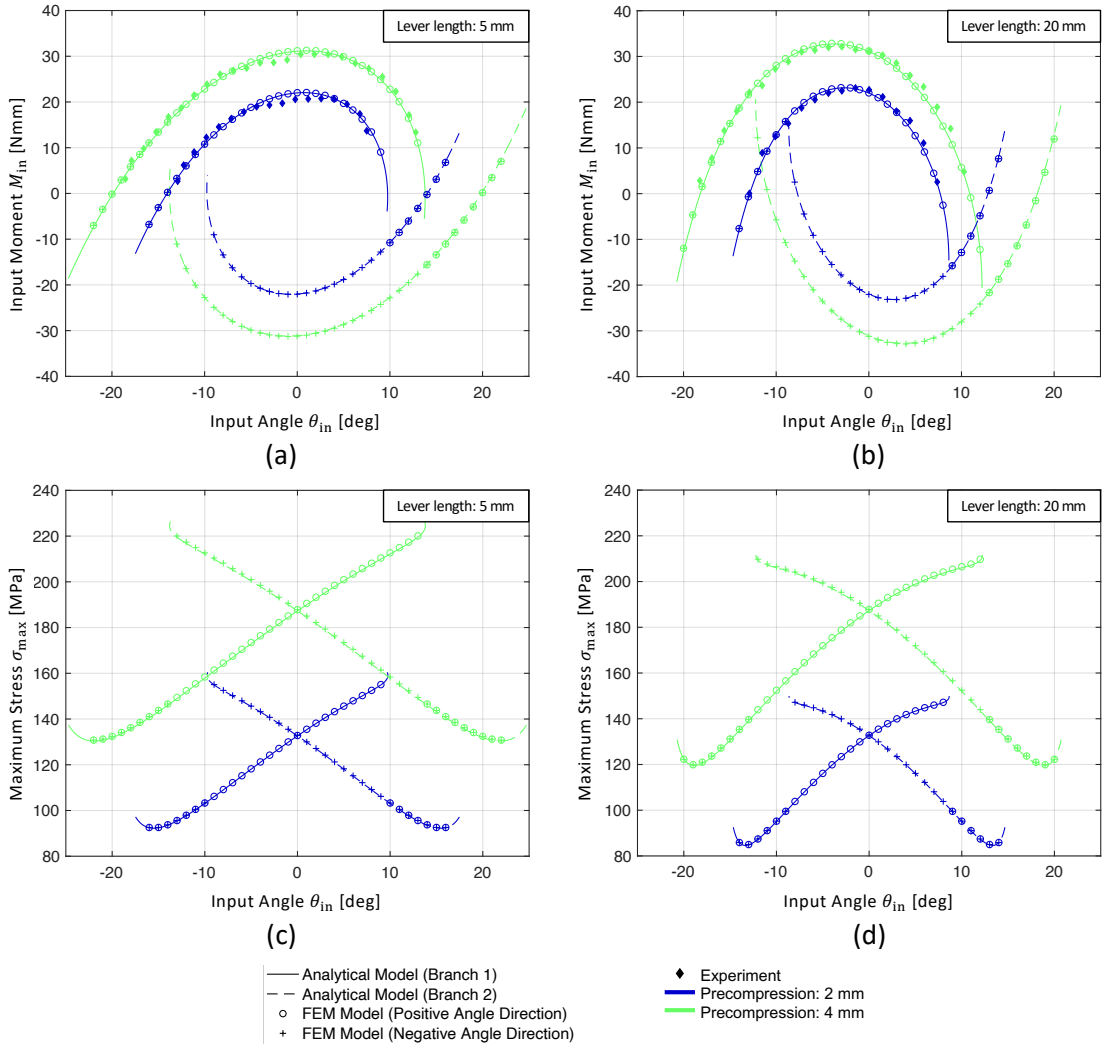

Figure 11. Single fixed-lever buckled beam actuation characteristics as a function of the input angle: (a-b) input moment, and (c-d) maximum stress for lever lengths of $p = 5$ mm ($\bar{p} = 2.5\%$) and $p = 20$ mm ($\bar{p} = 10\%$), respectively. See Fig. 2 for the position of the critical points.

6.2 Preloaded cross-spring pivot

The moment-angle characteristics of the preloaded cross-spring pivot is traced out in Fig. 12 using Eqs. (1), (2) and (9) for the symmetric and antisymmetric buckling configurations. The characteristics of the non-preloaded cross-spring pivot is also provided to observe the stiffness reduction.

For the antisymmetric buckling case, the analytical and FEM models show good agreement for the stable angle magnitude. Larger discrepancies appear for the angle limit, likely due to deformations of the rotating stage and to the fillets at the beam extremities, which were assumed infinitely rigid in the analytical model. Although the overall experimental behavior of the mechanism is well captured by the models, some discrepancies remain. We suppose that the preloading displacement is lower experimentally because the measured magnitudes of the stable angle θ_{stable}, the limit

angle $\theta_{\text{in,lim}}$ and the limit moment $M_{\text{in,lim}}$ are all approximately 5% lower than what was predicted by the analytical model for the antisymmetric buckling configuration. In contrast, the non-preloaded pivot matches the model predictions well.

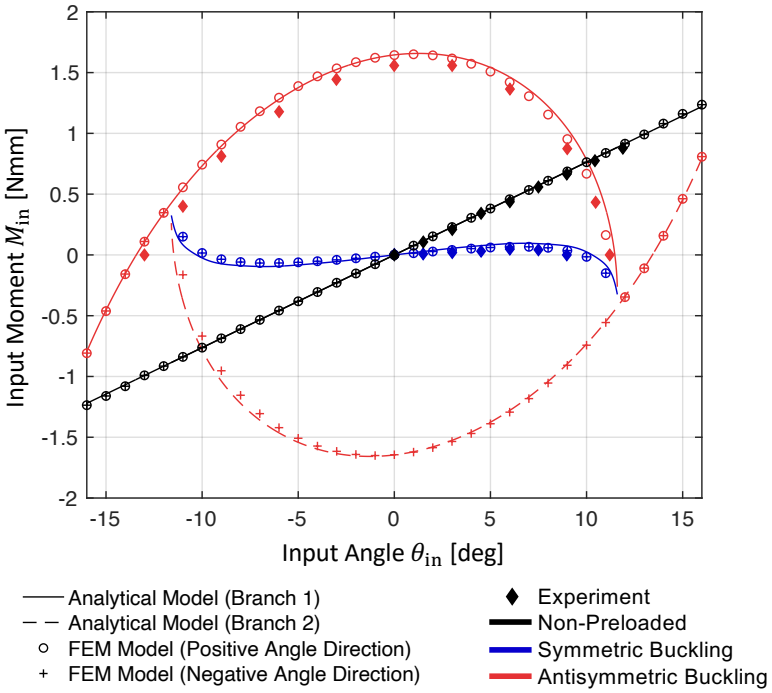

Figure 12. Moment-angle characteristics of the preloaded cross-spring pivot plastic mockup in comparison to the non-preloaded equivalent pivot.

A stiffness reduction of approximately 89% is obtained experimentally by comparing the maximum moment of the symmetric buckling pivot with that of the non-preloaded pivot at the same rotation amplitude. The reduction predicted by the models is lower: 75% from Eq. (8) and 81% from the FEM results. These discrepancies may stem from manufacturing tolerances, material creep, and measurement uncertainty. The symmetric buckling configuration also exhibits a smaller limit angle in the experiments than in the models. In this case, the stroke of the pivot is not limited by internal stress but by the angle limit points: if the input angle exceeds these limit points, the mechanism snaps from symmetric to antisymmetric buckling.

Remark 6: If mechanical end stops are placed between the second buckling mode and the corresponding angle limit, the pivot becomes tristable, with stable equilibria at the neutral position and at the two end stops. Such tristable behavior could benefit applications requiring low energy consumption, such as MEMS switches, relays, and microvalves (Chen et al., 2009; Chen and Du, 2012; Wang et al., 2014; Zhao et al., 2013).

6.3 Preloaded RCC pivot

The actuation results of the silicon RCC pivots are plotted in Fig. 13. Because the angular stroke of the RCC pivots is restricted to small amplitudes by mechanical stops

(±4.5 deg) that prevent snap-through into antisymmetric configurations, we linearize the analytical moment-angle curves. We thus treat the pivot stiffness (Eq. (15)) as constant for input angles near the neutral position. Specifically, we use the approximation $K_{\text{in,2beams}} \cong K_{\text{in,2beams,0}}$ as expressed in Eq. (8). Comparison of the FEM and experimental results with the linearized analytical model reveals only minor nonlinearities in the moment-angle characteristics.

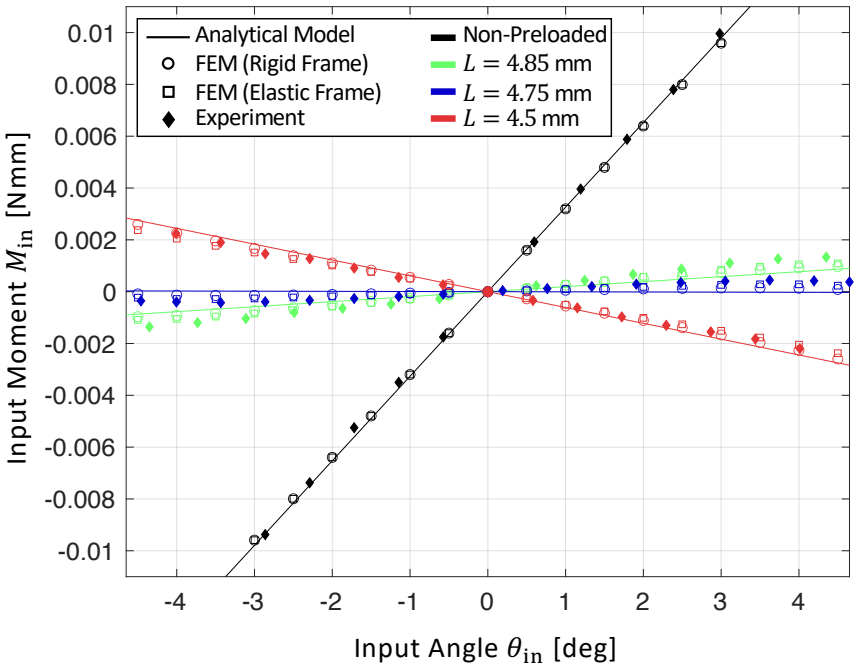

Figure 13. Moment-angle characteristics of the preloaded RCC pivot silicon prototypes in comparison to the non-preloaded equivalent pivot.

Figure 13 demonstrates that the results from both models and experiments are consistent with the expected behavior. Appropriate levels of stiffness reduction are observed when comparing the buckling beam lengths L. The experimental data show good agreement with the models for the non-preloaded pivot, with the relative difference in the input moment being below 6.7%. For the preloaded pivots, larger discrepancies are observed, likely due to manufacturing tolerances and potential plastic deformation arising during the cooling of the oxidized silicon wafer.

The analytical model aligns well with the FEM study assuming a rigid frame, as both models consider an infinitely stiff fixed frame. In contrast, the experimental results correspond more closely to the FEM analysis with an elastic frame, which better reflects the actual conditions. This highlights that the stiffness of the fixed frame must be accounted for in FEM simulations to achieve more accurate predictions of the rotational stiffness.

The concept of stiffness reduction is experimentally demonstrated. The preloaded RCC pivots exhibit measured stiffness reductions of 90% and 96% for buckling beam lengths of $L = 4.85$ mm and $L = 4.75$ mm, respectively. Additionally, it is shown that a bistable

flexure pivot with an approximately constant negative stiffness can be fabricated by using shorter buckling beams ($L = 4.5$ mm). As expected, the mechanical stops limit the angular stroke of this negative-stiffness pivot before reaching its angle limit points. This mechanism is therefore bistable, with the two stable positions occurring when the rotating stage contacts either of the end stops.

7 Conclusion

This paper presented the new approach for reducing the angular stiffness of flexure pivots using two centered fixed-lever post-buckled beams connected in parallel between a rotating stage and a fixed frame. The proposed architecture generates a negative stiffness that can be exploited to compensate for the intrinsic positive stiffness of generic flexure pivots. Depending on the beam geometry, preload conditions and the lever-arm distance, the resulting rotational stiffness can be designed to be positive, near-zero, or negative, while remaining nearly constant in the vicinity of the neutral position.

Beyond introducing a new pivot-preloading architecture, this work provides a predictive analytical framework for its synthesis. Closed-form analytical models were derived for the moment-angle behavior of single and paired post-buckled beams, enabling stiffness compensation to be designed in a single step, advancing from an iterative design process to a more predictable and controlled design process. The study further demonstrated that lever-arm geometry plays a central role in determining both the achievable stiffness reduction and angular stroke. In addition, the influence of secondary lever-arm effects arising when the buckled beams are offset relative to the pivot axis was identified and analytically quantified, clarifying an important geometric effect that substantially modifies the resulting angular stiffness.

The proposed analytical framework was illustrated through its application to representative flexure pivots, namely cross-spring and RCC pivots. Spring-steel and 3D-printed plastic mockups were designed, analyzed using finite element models, and experimentally characterized to validate the analytical predictions. Furthermore, recognizing the challenges associated with mechanical preloading at micro- and nanoscales, silicon monolithic pivots preloaded through thermal oxidation were investigated, demonstrating that the proposed concept is compatible with MEMS-scale fabrication.

Overall, the presented methodology establishes analytical design rules for stiffness-reduced flexure pivots and provides a predictable synthesis framework applicable across multiple pivot architectures, materials, and scales.

Future work will investigate the application of the proposed preloading strategy to silicon timekeeping oscillators, where stiffness reduction may be exploited to lower oscillation frequency while minimizing isochronism defects.

8 Acknowledgments

The authors thank Yves Pétremand, Michel Despont and Sylvain Nicolay from CSEM (Centre Suisse d'Electronique et Microtechnique) for their advice on the technological aspects of the design related to the silicon manufacturing process and for the execution of the manufacturing of all the silicon parts presented in this article (work done in the frame of bilateral EPFL-CSEM research collaboration).

9 References

Amoozandeh Nobaveh, A., Herder, J.L., Radaelli, G., 2024. Compliant variable negative to zero to positive stiffness twisting elements. Mech. Mach. Theory 196, 105607. https://doi.org/10.1016/j.mechmachtheory.2024.105607

Arredondo-Soto, M., Cuan-Urquizo, E., Gómez-Espinosa, A., 2021. A Review on Tailoring Stiffness in Compliant Systems, via Removing Material: Cellular Materials and Topology Optimization. Appl. Sci. 11. https://doi.org/10.3390/app11083538

Barents, R., Schenk, M., van Dorsser, W.D., Wisse, B.M., Herder, J.L., 2011. Spring-to-Spring Balancing as Energy-Free Adjustment Method in Gravity Equilibrators. J. Mech. Des. 133. https://doi.org/10.1115/1.4004101

Barri, K., Haughn, K.P.T., Henry, T.C., Phillips, F.R., Hrynuk, J.T., Mueller, J., 2025. Rotational bistable mechanisms for morphing wings and beyond. Commun. Eng. 4, 164. https://doi.org/10.1038/s44172-025-00495-2

Bilancia, P., Smith, S.P., Berselli, G., Magleby, S.P., Howell, L.L., 2020. Zero Torque Compliant Mechanisms Employing Pre-buckled Beams. J. Mech. Des. 142. https://doi.org/10.1115/1.4046810

Blad, T.W.A., van Ostayen, R.A.J., Tolou, N., 2021. A method for tuning the stiffness of building blocks for statically balanced compliant ortho-planar mechanisms. Mech. Mach. Theory 162, 104333. https://doi.org/10.1016/j.mechmachtheory.2021.104333

Chao, X., Hameed, I., Navarro-Alarcon, D., Jing, X., 2024. Untethered Bimodal Robotic Fish with Tunable Bistability, in: 2024 IEEE International Conference on Robotics and Automation (ICRA). pp. 1491–1497. https://doi.org/10.1109/ICRA57147.2024.10610967

Chen, G., Aten, Q.T., Zirbel, S., Jensen, B.D., Howell, L.L., 2009. A Tristable Mechanism Configuration Employing Orthogonal Compliant Mechanisms. J. Mech. Robot. 2. https://doi.org/10.1115/1.4000529

Chen, G., Du, Y., 2012. Double-Young Tristable Mechanisms. J. Mech. Robot. 5. https://doi.org/10.1115/1.4007941

Chen, T., Bilal, O.R., Shea, K., Daraio, C., 2018. Harnessing bistability for directional propulsion of soft, untethered robots. Proc. Natl. Acad. Sci. 115, 5698–5702. https://doi.org/10.1073/pnas.1800386115

Chi, Y., Li, Y., Zhao, Y., Hong, Y., Tang, Y., Yin, J., 2022. Bistable and Multistable Actuators for Soft Robots: Structures, Materials, and Functionalities. Adv. Mater. 34, e2110384. https://doi.org/10.1002/adma.202110384

Cosandier, F., Henein, S., Rubbert, L., Richard, M., 2017. Flexure Mechanism Design. EPFL Press.

de Laat, M.L.C., Pérez Garza, H.H., Herder, J.L., Ghatkesar, M.K., 2016. A review on in situ stiffness adjustment methods in MEMS. J. Micromechanics Microengineering 26, 063001. https://doi.org/10.1088/0960-1317/26/6/063001

Despont, M., Palmieri, M., Dubochet, O., Petremand, Y., 2020. Élément élastique pour un système micromécanique. CH718081B1.

Dijksman, J.F., 1979. A study of some aspects of the mechanical behaviour of cross-spring pivots and plate spring mechanisms with negative stiffness (Ph.D. thesis).

Dogan, O., 2022. Short-term Creep Behaviour of Different Polymers Used in Additive Manufacturing under Different Thermal and Loading Conditions. Stroj. Vestn. - J. Mech. Eng. 68, 451–460. https://doi.org/10.5545/sv-jme.2022.191

Halg, B., 1990. On a nonvolatile memory cell based on micro-electro-mechanics, in: IEEE Proceedings on Micro Electro Mechanical Systems, An Investigation of Micro Structures, Sensors, Actuators, Machines and Robots. pp. 172–176. https://doi.org/10.1109/MEMSYS.1990.110271

Henein, S., 2000. Conception des structures articulées à guidages flexibles de haute précision (Ph.D. thesis). EPFL. https://doi.org/10.5075/epfl-thesis-2194

Howell, L.L., 2001. Compliant Mechanisms. John Wiley & Sons.

Hussein, H., Khan, F., Younis, M.I., 2020. A symmetrical bistable mechanism from combination of pre-shaped microbeams. Sens. Actuators Phys. 306, 111961. https://doi.org/10.1016/j.sna.2020.111961

Hussein, H., Wang, C., Amendoeira Esteves, R., Kraft, M., Fariborzi, H., 2024. Near-zero stiffness accelerometer with buckling of tunable electrothermal microbeams. Microsyst. Nanoeng. 10, 43. https://doi.org/10.1038/s41378-024-00657-w

Kuppens, P.R., Bessa, M.A., Herder, J.L., Hopkins, J.B., 2021a. Monolithic binary stiffness building blocks for mechanical digital machines. Extreme Mech. Lett. 42, 101120. https://doi.org/10.1016/j.eml.2020.101120

Kuppens, P.R., Bessa, M.A., Herder, J.L., Hopkins, J.B., 2021b. Compliant Mechanisms That Use Static Balancing to Achieve Dramatically Different States of Stiffness. J. Mech. Robot. 13. https://doi.org/10.1115/1.4049438

Kuppens, P.R., Herder, J.L., Tolou, N., 2019. Permanent Stiffness Reduction by Thermal Oxidation of Silicon. J. Microelectromechanical Syst. 28, 900–909. https://doi.org/10.1109/JMEMS.2019.2935379

Liang, H., Hao, G., Olszewski, O.Z., Pakrashi, V., 2022. Ultra-low wide bandwidth vibrational energy harvesting using a statically balanced compliant mechanism. Int. J. Mech. Sci. 219, 107130. https://doi.org/10.1016/j.ijmecsci.2022.107130

Liu, T., Bi, S., Yao, Y., Dong, Z., Yang, Q., Liu, L., 2020. Research on zero-stiffness flexure hinge (ZSFH) based on spring four-bar linkage(4BSL). Mech. Mach. Theory 143, 103633. https://doi.org/10.1016/j.mechmachtheory.2019.103633

Liu, T., Hao, G., 2025. Comprehensive SCME: A nonlinear large-deformation modeling approach for planar compliant mechanisms. Mech. Mach. Theory 213, 106070. https://doi.org/10.1016/j.mechmachtheory.2025.106070

Ma, Z., Zhou, R., Yang, Q., 2022. Recent Advances in Quasi-Zero Stiffness Vibration Isolation Systems: An Overview and Future Possibilities. Machines 10. https://doi.org/10.3390/machines10090813

Mauser, K., Hasse, A., 2020. How to prestress compliant mechanisms for a targeted stiffness adjustment. Smart Mater. Struct. 29, 085021. https://doi.org/10.1088/1361-665X/ab9237

Mauser, K., Sjarov, M., Nowak, A., Campanile, L.F., Hasse, A., 2022. Design and control of actively prestressed compliant mechanisms for variable stiffness actuators. J. Intell. Mater. Syst. Struct. 33, 2422–2439. https://doi.org/10.1177/1045389X221085656

Merriam, E.G., Bruton, J.T., Magleby, S.P., Howell, L.L., 2016. A Method for Determining Load-Dependent Stiffness of Flexures, in: ASME 2015 International Design Engineering Technical Conferences and Computers and Information in Engineering Conference. https://doi.org/10.1115/DETC2015-46628

Morsch, F.M., Herder, J.L., 2011. Design of a Generic Zero Stiffness Compliant Joint, in: ASME 2010 International Design Engineering Technical Conferences and Computers and Information in Engineering Conference. pp. 427–435. https://doi.org/10.1115/DETC2010-28351

Niazi, M.U.K., Mehmood, U., Choi, J., Lee, Y.S., Moon, Y., 2026. Custom Shape Formation in Continuum Robots Using Compliant Bistable Segments for Medical Applications. Adv. Intell. Syst. 8, 2500512. https://doi.org/10.1002/aisy.202500512

Numić, A., Blad, T.W.A., van Keulen, F., 2021. Effect of Matching Buckling Loads on Post-Buckling Behavior in Compliant Mechanisms, in: ASME 2021 International Design Engineering Technical Conferences and Computers and Information in Engineering Conference. https://doi.org/10.1115/DETC2021-68439

Pan, D., Shen, Y., Huang, C., Wu, Z., 2022. Analysis of snap-through behavior of bistable buckled beam under end-moment static actuation. Int. J. Non-Linear Mech. 142, 103937. https://doi.org/10.1016/j.ijnonlinmec.2022.103937

Pan, D., Tan, S., Zhang, Z., Li, W., 2025. The metastructures actuated by rotational motion with quasi-zero stiffness, negative stiffness, and bistability. Thin-Walled Struct. 207, 112700. https://doi.org/10.1016/j.tws.2024.112700

Parkinson, B., Jensen, B.D., Howell, L.L., Magleby, S.P., 2025. Considering Boundary Conditions in the Design of Compliant Mechanisms With Desired Force Profiles. J. Mech. Des. 147. https://doi.org/10.1115/1.4068231

Qiu, J., Lang, J.H., Slocum, A.H., 2004. A curved-beam bistable mechanism. J. Microelectromechanical Syst. 13, 137–146. https://doi.org/10.1109/JMEMS.2004.825308

Saif, M.T.A., 2000. On a tunable bistable MEMS-theory and experiment. J. Microelectromechanical Syst. 9, 157–170. https://doi.org/10.1109/84.846696

Smith, S.T., 2000. Flexures: Elements of Elastic Mechanisms. CRC Press.

Smreczak, M., Tissot-Daguette, L., Thalmann, E., Baur, C., Henein, S., 2022. A load cell with adjustable stiffness and zero offset tuning dedicated to electrical micro- and nanoprobing. Precis. Eng. 76, 208–225. https://doi.org/10.1016/j.precisioneng.2022.03.009

Spanoudakis, P., Kiener, L., Cosandier, F., Schwab, P., Giriens, L., Kruis, J., Grivon, D., Psoni, G., Vrettos, C., Bencheikh, N., 2019. Large angle flexure pivot development for future science payloads for space applications. MATEC Web Conf. 304, 07016. https://doi.org/10.1051/matecconf/201930407016

Tang, Y., Chi, Y., Sun, J., Huang, T.-H., Maghsoudi, O.H., Spence, A., Zhao, J., Su, H., Yin, J., 2020. Leveraging elastic instabilities for amplified performance: Spine-inspired high-speed and high-force soft robots. Sci. Adv. 6, eaaz6912. https://doi.org/10.1126/sciadv.aaz6912

Thalmann, E., Henein, S., 2022. Triple Crossed Flexure Pivot Based on a Zero Parasitic Center Shift Kinematic Design. J. Mech. Robot. 14. https://doi.org/10.1115/1.4053471

Thalmann, E., Kahrobaiyan, M.H., Vardi, I., Henein, S., 2020. Flexure Pivot Oscillator With Intrinsically Tuned Isochronism. J. Mech. Des. 142, 075001. https://doi.org/10.1115/1.4045388

Tissot-Daguette, L., Cosandier, F., Gubler, Q., Pétremand, Y., Despont, M., Henein, S., 2025. Residual stress chevron preloading amplifier for large-stroke stiffness reduction of silicon flexure mechanisms. J. Micromechanics Microengineering 35, 025003. https://doi.org/10.1088/1361-6439/ada165

Tissot-Daguette, L., Cosandier, F., Thalmann, E., Henein, S., 2024a. Near-Zero Parasitic Shift Flexure Pivots Based on Coupled n-RRR Planar Parallel Mechanisms. J. Mech. Robot. 16. https://doi.org/10.1115/1.4065074

Tissot-Daguette, L., Prêcheur-Llarena, S.H., Baur, C., Henein, S., 2024b. Fully compliant snap-through bistable gripper mechanism based on a pinned-pinned buckled beam, in: Euspen 24th International Conference & Exhibition. Dublin, IE.

Tissot-Daguette, L., Schneegans, H., Gubler, Q., Baur, C., Henein, S., 2022a. Rectilinear translation four-bar flexure mechanism based on four Remote

Center Compliance pivots, in: Euspen 22nd International Conference & Exhibition. Geneva, CH.

Tissot-Daguette, L., Schneegans, H., Thalmann, E., Henein, S., 2022b. Analytical modeling and experimental validation of rotationally actuated pinned–pinned and fixed–pinned buckled beam bistable mechanisms. Mech. Mach. Theory 174, 104874. https://doi.org/10.1016/j.mechmachtheory.2022.104874

Tissot-Daguette, L., Smreczak, M., Baur, C., Henein, S., 2021. Load cell with adjustable stiffness based on a preloaded T-shaped flexure pivot, in: Euspen 21st International Conference & Exhibition. Copenhagen, DK.

Vangbo, M., Bäcklund, Y., 1998. A lateral symmetrically bistable buckled beam. J. Micromechanics Microengineering 8, 29. https://doi.org/10.1088/0960-1317/8/1/005

Wang, D.-A., Chen, J.-H., Pham, H.-T., 2014. A tristable compliant micromechanism with two serially connected bistable mechanisms. Mech. Mach. Theory 71, 27–39. https://doi.org/10.1016/j.mechmachtheory.2013.08.018

Wen, K., Wu, G., 2025. Design and Analysis of a Serial Position-Controlled Variable Stiffness Rotating Mechanism Based on Multi-Stage Torsional Compliant Mechanisms. Actuators 14. https://doi.org/10.3390/act14050236

Wu, Y.-S., Lan, C.-C., 2014. Linear Variable-Stiffness Mechanisms Based on Preloaded Curved Beams. J. Mech. Des. 136. https://doi.org/10.1115/1.4028705

Yang, Q., Bi, S., Liu, T., 2020. Static balancing of flexural pivots with two symmetrically arranged pre-compressing springs. IOP Conf. Ser. Mater. Sci. Eng. 892, 012121. https://doi.org/10.1088/1757-899X/892/1/012121

Yang, Y.-J., Liao, B.-T., Kuo, W.-C., 2007. A novel 2 × 2 MEMS optical switch using the split cross-bar design. J. Micromechanics Microengineering 17, 875. https://doi.org/10.1088/0960-1317/17/5/005

Yu, B., Liao, H., Xie, X., Li, B., Fan, D., Xie, M., Han, D., 2025. A novel bidirectional negative stiffness mechanism based on compliant curved beams for shock isolation. Results Eng. 28, 108255. https://doi.org/10.1016/j.rineng.2025.108255

Zanaty, M., Fussinger, T., Rogg, A., Lovera, A., Lambelet, D., Vardi, I., Wolfensberger, T.J., Baur, C., Henein, S., 2019. Programmable Multistable Mechanisms for Safe Surgical Puncturing. J. Med. Devices 13. https://doi.org/10.1115/1.4043016

Zanaty, M., Vardi, I., Henein, S., 2018. Programmable Multistable Mechanisms: Synthesis and Modeling. J. Mech. Des. 140. https://doi.org/10.1115/1.4038926

Zhao, H., Bi, S., 2010. Accuracy characteristics of the generalized cross-spring pivot. Mech. Mach. Theory 45, 1434–1448. https://doi.org/10.1016/j.mechmachtheory.2010.05.004

Zhao, H., Han, D., Zhang, L., Bi, S., 2017. Design of a stiffness-adjustable compliant linear-motion mechanism. Precis. Eng. 48, 305–314. https://doi.org/10.1016/j.precisioneng.2016.12.013

Zhao, H., Zhao, C., Ren, S., Bi, S., 2019. Analysis and evaluation of a near-zero stiffness rotational flexural pivot. Mech. Mach. Theory 135, 115–129. https://doi.org/10.1016/j.mechmachtheory.2019.02.003

Zhao, J., Gao, R., Yang, Y., Huang, Y., Hu, P., 2013. A Bidirectional Acceleration Switch Incorporating Magnetic-Fields-Based Tristable Mechanism. IEEEASME Trans. Mechatron. 18, 113–120. https://doi.org/10.1109/TMECH.2011.2163725

Zirbel, S.A., Tolman, K.A., Trease, B.P., Howell, L.L., 2016. Bistable Mechanisms for Space Applications. PLOS ONE 11, e0168218. https://doi.org/10.1371/journal.pone.0168218